AGU PUBLICATIONS

JGR

Journal of Geophysical Research: Solid Earth

RESEARCH ARTICLE

10.1002/2014JB011664

Key Points:

- Single-sidedness of subduction is more stable with a low yield strength crust
- A strong slab and a low-viscosity asthenosphere promote subduction longevity
- Subduction polarity reversal and its shut-off and slab break-off are observed

Supporting Information:

- Figures S1–S3
- Movie S1

Correspondence to:
F. Crameri,
f.crameri@ucl.ac.uk

Citation:
Crameri, F., and P. J. Tackley (2015), Parameters controlling dynamically self-consistent plate tectonics and single-sided subduction in global models of mantle convection, *J. Geophys. Res. Solid Earth*, *120*, doi:10.1002/2014JB011664.

Received 7 OCT 2014
Accepted 26 MAR 2015
Accepted article online 30 MAR 2015

Parameters controlling dynamically self-consistent plate tectonics and single-sided subduction in global models of mantle convection

Fabio Crameri[1,2] and Paul J. Tackley[2]

[1]Department of Earth Sciences, University College London, London, UK, [2]Department of Earth Sciences, ETH Zurich, Zurich, Switzerland

Abstract Recent advances in numerical modeling allow global models of mantle convection to more realistically reproduce the behavior at convergent plate boundaries; in particular, the inclusion of a free surface at the outer boundary has been shown to facilitate self-consistent development of single-sided subduction. This allows for a more extensive study of subduction in the context of global mantle convection, as opposed to commonly used regional models. Our first study already indicated important differences between mantle convection with single-sided subduction and mantle convection with double-sided subduction. Here we further investigate the effect of various physical parameters and complexities on inducing Earth-like plate tectonics and its evolution in time. Results reinforce the previous finding that using a free surface instead of a free-slip outer boundary dramatically changes subduction style, with free surface cases displaying many episodes of single-sided subduction, which leads to more realistic slab dip, stress state, trench retreat rate, and slab-induced mantle flow. Longevity of single-sided subduction is promoted by a layer of hydrated crust with a low yield strength to lubricate the subduction channel, a low-viscosity asthenosphere, and a high strength of the slab (determined by a combination of high-diffusion creep viscosity and intermediate friction coefficient), although its effective viscosity is in the observationally constrained range in the bending region. The time evolution displays interesting events including subduction polarity reversals, subduction shut-off, and slab break-off.

1. Introduction

Understanding the origin of plate tectonics in a convecting mantle, and thus obtaining self-consistently emerging mobile surface plates in mantle convection simulations, is a long-standing challenge. The majority of mantle convection models featuring a mobile lid thus impose some aspect such as plate velocity, trench velocity, or weak zones [see *Bercovici et al.*, 2000; *Lowman*, 2011, and references therein]. In order to understand the formation and development of plate boundaries, it is, however, important to incorporate the relevant physical properties into the model itself so that plates form and develop self-consistently. One physical complexity that was recently shown to be important in time-dependent mantle convection with strongly temperature and pressure dependent, viscoplastic rheology is a free surface at the outer boundary: with this, single-sided subduction like that found in nature often emerges self-consistently, whereas when the commonly used free-slip boundary condition is instead applied, subduction is normally symmetric (double-sided) [*Crameri et al.*, 2012a]. This present study aims to further investigate the influence of various physical properties and complexities on subduction behavior in such a model. In the remaining parts of this section, the relevant observations and previous modeling studies are briefly discussed.

1.1. Observations

Subduction zones on present-day Earth are distinctive asymmetric features consisting of a subducting plate dipping into the mantle and thereby underthrusting an overlying plate that remains at the surface [e.g., *Amstutz*, 1955; *Wortel and Spakman*, 2000; *King*, 2001; *Zhao*, 2004], although the occurrence and characteristics of subduction zones is still debated for the early Archean Earth [*Davies and Stevenson*, 1992; *de Wit*, 1998; *Sizova et al.*, 2010; *van Hunen and van den Berg*, 2008]. Convergent plate boundaries are subdivided into three categories: ocean-ocean zones (e.g., Mariana subduction zone), ocean-continent zones (e.g., South America subduction zone) and continent-continent zones (e.g., India-Eurasia collision). Here we consider only the first type of convergent plate boundary by simply not including continents.

A wide variety of dynamical behavior is observed in subduction zones. The subduction mode can vary in space (i.e., along strike) and time, even along a single subduction zone [*Lallemand et al.*, 2005; *Sdrolias and Müller*, 2006]. Key differences in modes can be observed in the upper plate, at the trench, and also at the upper to lower mantle transition zone: The stress state in the upper plate ranges from compression to extension, trench motion varies between the advancing and the (more often observed) retreating mode [*Schellart et al.*, 2008], and finally, the sinking of slabs varies from stagnation in the transition zone to direct penetration into the lower mantle [*Bijwaard et al.*, 1998; *Fukao et al.*, 2001].

1.2. Regional Modeling

The dynamics of subduction has been intensively studied using regional models [see *Gerya*, 2011, and references therein]. Using laboratory experiments or numerical models, "free subduction," in which a single plate initially lying at the surface is free to subduct, has been found to be able to produce the diverse subduction modes mentioned above depending on the density and rheology of the subducting plate [*Bellahsen et al.*, 2005; *Schellart*, 2008b; *Stegman et al.*, 2010; *Ribe*, 2010]. Further studies on subduction dynamics using regional numerical models highlighted the importance of bending and downgoing plate properties [*Capitanio et al.*, 2007, 2009]. It was shown that subducting plates minimize their overall dissipation rate by adjusting their bending curvature at the subduction zone [*Capitanio et al.*, 2007; *Schellart*, 2009; *Irvine and Schellart*, 2012]. Even in the presence of a strong core (i.e., cross-sectional plate interior), plates only weakly resist bending and generally propagate a large amount (i.e., 75–80%) of slab pull from depth to the surface.

Other regional studies focused on the upper plate, which has been found to be able to produce time-dependent subduction behavior and to modify the velocity and morphology of the sinking plate [*De Franco et al.*, 2007; *Clark et al.*, 2008; *Capitanio et al.*, 2010; *van Dinther et al.*, 2010; *Capitanio et al.*, 2011; *van Hunen and Allen*, 2011; *Butterworth et al.*, 2012; *Meyer and Schellart*, 2013; *Garel et al.*, 2014]. Some work has investigated the interaction of slabs resulting from two adjacent subduction zones [*Mishin et al.*, 2008; *Yamato et al.*, 2009]. However, despite the success of regional models, modeling subduction in the framework of mantle convection is important for a complete understanding of the dynamics involved in this process.

1.3. Global Modeling

A major challenge in modeling mantle convection at the global scale is to self-consistently generate a mobile-lid style of tectonics. Strongly temperature-dependent viscosity is a key ingredient for a realistic model of plate tectonics, yet it is not sufficient by itself to create mobile plates, rather leading to a stagnant lid that does not participate in the convective overturn of the mantle [*Nataf and Richter*, 1982; *Stengel et al.*, 1982; *Solomatov*, 1995; *Ratcliff et al.*, 1997]. Initial attempts to investigate the influence of plates on mantle convection therefore involved the a priori imposition of features characterizing plate tectonics. In many models, the surface velocity or surface stresses were specified [e.g., *Chase*, 1979; *Hager and O'Connell*, 1979; *Bunge and Richards*, 1996; *Monnereau and Quéré*, 2001; *King et al.*, 2002; *Gait et al.*, 2008], or artificial weak zones in the lithosphere were introduced [e.g., *Schmeling and Jacoby*, 1981; *Gurnis*, 1988; *Davies*, 1989; *King and Hager*, 1990; *Puster et al.*, 1995; *Zhong and Gurnis*, 1995].

Modeling attempts without any imposed features successfully produced plate boundaries by adding plastic yielding, i.e., applying a viscoplastic rheology. This allows for the dynamically self-consistent generation of plate-like behavior in global models of mantle convection [*Moresi and Solomatov*, 1998; *Trompert and Hansen*, 1998; *Tackley*, 2000a, 2000b; *Stein et al.*, 2004; *van Heck and Tackley*, 2008; *Foley and Becker*, 2009], although the resulting plate boundaries are relatively broad and subduction is typically double-sided. Global three-dimensional models with a free surface were presented by *Crameri and Tackley* [2014] and demonstrated the propensity to generate single-sided subduction. A limitation of all of these models is that the value of yield stress or friction coefficient (see equation (6)) necessary to obtain plate-like behavior is 0.5–1 order of magnitude smaller than that measured in laboratory experiments; the presence of continents reduces this gap [*Rolf and Tackley*, 2011], and a free surface also allows subduction to initiate more readily [*Crameri*, 2013].

Plate tectonics as operating on Earth, however, involves strong deformation in strongly localized, narrow zones of the lithosphere. There, faulting occurs in the brittle (and elastic) upper part, which transitions to ductile shearing in the lower lithosphere. Such shear zones are thought to be caused by one or more strain-induced weakening mechanisms like grain size reduction [*Karato et al.*, 1980, 1986; *Bercovici and Ricard*, 2005; *Rozel et al.*, 2011; *Bercovici and Ricard*, 2013; *Foley and Bercovici*, 2014], void generation

[*Bercovici*, 1998; *Regenauer-Lieb*, 1998], shear heating [*Yuen et al.*, 1978; *Crameri and Kaus*, 2010; *Thielmann and Kaus*, 2012], or pore fluid pressure [*Dymkova and Gerya*, 2013]. The addition of water or melt into the lithosphere also has a weakening effect [*Hirth and Kohlstedt*, 2003]. Once subduction has been initiated, a lithosphere-scale weak channel maintained by such a mechanism and/or by actual weak sediment that has been advected down into the subduction zone is thought to be key in inducing realistic, single-sided subduction by providing lubrication at the plate interface [*Lenardic and Kaula*, 1994; *Tagawa et al.*, 2007; *Gerya et al.*, 2008; *Crameri et al.*, 2012a; *Duarte et al.*, 2013; *Dymkova and Gerya*, 2013].

The dynamics of realistic plate tectonics are, however, governed not only by the rheology of the mantle's interior but also by its boundaries. The most important boundary is probably the rock-air/water interface, which has recently been shown to be important for allowing a natural bending (i.e., not altered by a fixed flat surface) of the slab [*Kaus et al.*, 2010] and key in producing Earth-like single-sided subduction [*Crameri et al.*, 2012a]. In numerical models employing a fixed Eulerian grid, which is the most common type of grid used in global mantle convection studies, the surface is most conveniently defined to correspond to a horizontal row of grid points at the top of the numerical model domain. This procedure, however, enforces a flat surface on top of the convecting mantle. Although topography is small compared to the dominant length scale of mantle convection, a freely evolving surface topography is important for subducting plates: a foreland bulge and, more importantly, a deep trench lead to a more natural plate bending at the collision zone. This prevents unnatural plate weakening and, together with a weak hydrated crust [*Gerya et al.*, 2008], thus keeps the strongly deforming subduction channel localized. The convergence of two strong plates (fostered by a free surface) along a weak, localized shear zone (fostered by a weak hydrated crustal layer) therefore produces single-sided subduction self-consistently [*Crameri et al.*, 2012a].

A global model of mantle convection with such realistic subduction dynamics allows for a more extensive study of plate tectonics that, in contrast to the numerous regional models, incorporates the complete framework of mantle convection.

2. Model and Method

2.1. Physical Model

We here assume an incompressible mantle under the Boussinesq approximation, for which the relevant nondimensional equations for conservation of mass, momentum, and energy are

$$\vec{\nabla} \cdot \vec{v} = 0 \tag{1}$$

$$\vec{\nabla} \cdot \sigma_{ij} - \vec{\nabla} p = RaT\hat{\vec{e}}_z \tag{2}$$

$$\frac{\partial T}{\partial t} = \nabla^2 T - \vec{v} \cdot \vec{\nabla} T + H \tag{3}$$

where v is the velocity, σ_{ij} is the deviatoric stress tensor, p is the pressure, T is the temperature, $\hat{\vec{e}}_z$ is the vertical unit vector, t is the time, and H is the nondimensional internal heating rate. The temperature-based Rayleigh number (Ra) can be expressed in terms of density (ρ), gravitational acceleration (g), temperature scale (ΔT), mantle depth (D), thermal diffusivity (κ), and reference viscosity (η_0) as

$$Ra = \frac{\rho g \alpha \Delta T D^3}{\eta_0 \kappa} \tag{4}$$

The assumed temperature-based Rayleigh number is 10^6, and the nondimensional internal heating rate is 20.0, which gives an internal heating-based Rayleigh number of 2.0×10^7. The assumed rheology is strongly temperature- and pressure-dependent:

$$\eta(T,p) = \eta_0 \cdot \exp\left[\frac{E_{\mathrm{act}} + pV_{\mathrm{act}}}{RT}\right] \tag{5}$$

where η is the viscosity, p is the pressure, $R = 8.314\,\mathrm{J\,mol^{-1}\,K^{-1}}$ is the gas constant, T is the temperature, $E_{\mathrm{act}} = 240\,\mathrm{kJ\,mol^{-1}}$ is the activation energy, V_{act} is the varied activation volume, and η_0 is set such that η

10.1002/2014JB011664

Table 1. Parameters Used in This Study

Parameter	Symbol	Nondimensional Value	Dimensional Value
Reference viscosity	η_0	1	10^{23} Pa s
Mantle depth	D	1	2890 km
Gravitational acceleration	g	-	9.81 ms^{-2}
Thermal conductivity	k	-	3 W $\mathrm{m}^{-1}\mathrm{K}^{-1}$
Thermal diffusivity	κ	1	10^{-6} $\mathrm{m}^2\,\mathrm{s}^{-1}$
Thermal expansivity	α	-	3×10^{-5} K^{-1}
Temperature gradient	ΔT	1	2500 K
Reference density	ρ_0	1	3300 kg m^{-3}
Heat capacity	Cp_0	-	1200 J kg^{-1} K^{-1}
Internal heating rate	H	20	5.44×10^{-12} W kg^{-1}
Activation energy	E_{act}	11.55	240 kJ mol^{-1}
Activation volume	V_{act}	3.0 [a]	6.34×10^{-7} m^3 mol[a]
Friction coefficient	μ	0.1 [a]	-
Cohesion	C	1577 [a]	10^7 Pa[a]
Upper viscosity cutoff	η_{max}	$10^5\eta_0$	10^{28} Pa s
Lower viscosity cutoff	η_{min}	$10^{-4}\eta_0$	10^{19} Pa s
		Sticky air layer[b]	
Thickness	d_{st}	0.05	145 km
Viscosity	η_{st}	$10^{-3}\eta_0$ [a]	10^{20} Pa s[a]
		Weak crustal layer[b]	
Thickness	d_{crust}	0.006[c]	18 km[c]
Viscosity	η_{crust}	η_0	10^{23} Pa s
Friction coefficient	μ_{crust}	0.001[a]	-
Cohesion	C_{crust}	158	10^6 Pa

[a]Indicated is the standard setup. Parameter variation is mentioned separately.
[b]If applied.
[c]Dependent on vertical resolution. Given is the maximum value applied.

gives the reference viscosity at $T = 1600$ K and $p = 0$ Pa. Additionally, plastic yielding is included by a yield stress limiter using a Drucker-Prager yield criterion with the pressure-dependent yield stress σ_y based on Byerlee's law

$$\sigma_y = C + p\mu \tag{6}$$

with specified friction coefficient μ and cohesion C. If plastic yielding occurs, the effective viscosity on the corresponding grid points becomes $\eta_{eff} = \min[\eta(T,p), \eta_y]$ with $\eta_y = \sigma_y/2\dot{\epsilon}$. Finally, the viscosity variation is limited to 9 orders of magnitude by applying an upper and lower cutoff of $\eta_{max} = 10^5\eta_0$ and $\eta_{min} = 10^{-4}\eta_0$. In some cases a weak hydrated crustal layer is included. Material of the weak crustal layer is assumed to become "weak crust" by reducing the viscosity and/or the yield stress (see section 3.4.2) after it has resided in the uppermost part of the solid Earth for a time period of $t > 25$ ka. The layer's thickness depends on the vertical resolution and is such that the layer spans three grid points with $d_{crust} = 18$ km and $d_{crust} = 9$ km for $nz = 128$ and $nz = 256$ vertical grid points, respectively. The weak crust (differing from mantle material only in its viscosity and/or yield strength) is converted to regular mantle again when subducted below a depth of $d > 900$ km. The model is purely internally heated (using an internal heating rate of 5.44×10^{-12} W kg^{-1}). The domain depth is intended to represent the whole mantle depth. The top boundary (including the air layer if applied) is set to a constant 300 K, while the bottom boundary is insulating by applying a zero heat flux condition. Top and bottom model domain boundaries are free-slip (whereas the actual rocky surface can be allowed to be a free surface by adding an air layer as mentioned below), and side boundaries are periodic to minimize boundary effects on subduction and the induced mantle flow: the flow in the narrow 2:1 model

Table 2. Model Setups Presented in This Study

Tag	Top Boundary	Resolution ($nx \times nz$)	Activation Volume (V_{act}) [nd]	Cohesion (C) [nd]	Friction Coefficient (μ) [nd]	Weak Hydrated Crust: Cohesion (C_{crust}) [nd]	Weak Hydrated Crust: Viscosity Difference ($\Delta\eta$) [nd]	Weak Hydrated Crust: Friction Coefficient (μ_{crust}) [nd]	MVR[a] Solidus Temperature ($T_{sol,0}$) [nd]
regime1	sticky air	256×128	4.0	100	variable	100	10^{-2}	0.09	-
regime2	sticky air	256×128	variable	100	0.09	100	10^{-2}	0.09	-
topBC1	free-slip	512×256	3.0	100	0.1	-	-	-	-
topBC2	sticky air	512×256	3.0	100	0.1	-	-	-	-
topBC3	sticky air	512×256	3.0	1577	0.1	158	0	0.001	-
topBC4	free-slip	512×256	3.0	1577	0.1	158	0	0.001	-
standard	sticky air	512×256	3.0	1577	0.1	158	0	0.001	0.6
comp	sticky air	512×256	3.0	100	0.1	1577	10^{-1}	0.001	-
mvr	sticky air	512×256	3.0	1577	0.1	158	0	0.001	0.5

[a]MVR: melting viscosity reduction (see section 3.4.5).

domain is less perturbed by periodic boundaries than by two vertical free-slip walls, which tend to guide the location of subduction and make it vertical. Further physical and numerical parameter details are given in Table 1.

2.2. Numerical Model

Calculations are performed in two-dimensional Cartesian geometry with an aspect ratio of 2:1 ($x : z$) to allow for efficient computation at high resolution. The physical model described above is solved by the finite difference/volume multigrid code StagYY [e.g., *Tackley*, 2008]. Three types of nondiffusive tracers are advected with the flow and track the composition, which is either mantle, weak crust, or air.

The model domain consists of the whole mantle depth plus (for free surface cases) a “sticky air” layer on top [*Matsumoto and Tomoda*, 1983; *Schmeling et al.*, 2008]. The sticky air approach simulates a free surface in models calculated on a Eulerian grid. This weak layer consists of an isothermal, low-viscosity “air” of (nearly) zero density that decouples the surface of the lithosphere from the free-slip top of the model domain. For a good free surface treatment this air layer has to be sufficiently thick and has to have sufficiently low viscosity [*Crameri et al.*, 2012b]. Using actual values of air or water viscosity is computationally unfeasible, but tests show that a viscosity of $\sim 10^{19}$ Pa s with a thickness of 150 km is sufficient (see also section 3.4.6). This leads to typical density and viscosity contrasts between surface rocks and air of around 3300–3400 kg/m^3 and $10^1 - 10^4$ Pa s, respectively. The temperature of the air is set to the surface boundary temperature of 300 K.

The thin subduction channel has to be resolved properly to a depth greater than the base of the lithosphere in order to guarantee lubrication between the converging plates. This requires a high number of vertical grid points. We performed resolution tests using up to 512 vertical grid points (nz), including vertical grid refinement, as shown in supporting information Figure S1. These show that to ensure the fidelity of the dynamical processes that are of interest in this work, $nz > 64$ is needed if the grid is vertically refined at shallow depth (i.e., more than three grid points across the weak crustal layer). For the majority of the models presented here (e.g., for the model “standard”) we use 2 times as many points (see Table 2).

2.3. Dimensional Scaling

The results obtained in this study are calculated using nondimensional values and parameters (see also Table 1). The characteristic viscosity η_0 is derived from the Rayleigh number Ra_0 assuming “realistic” values of all other parameters and given by

$$\eta_0 = \frac{\rho_0 \cdot g \cdot \alpha \cdot \Delta T \cdot D^3}{\kappa \cdot Ra_0} \tag{7}$$

where ρ_0 is the reference density, g is the gravitational constant, α is the thermal expansivity, D is the mantle depth, and κ is the thermal diffusivity. The temperature scale ΔT is the temperature assumed to be $\Delta T = 1$ nondimensionally. Nondimensional times are dimensionalized using the thermal diffusion timescale

10.1002/2014JB011664

$$t_{\text{diff}} = \frac{D^2}{\kappa} \tag{8}$$

the stress scale $\Delta\sigma$ is

$$\Delta\sigma = \eta_0 \frac{\kappa}{D^2} \tag{9}$$

and the internal heating rate is dimensionalized using the heating scale

$$\Delta H = \frac{\kappa C p_0 \Delta T}{D^2} \tag{10}$$

where Cp_0 is the reference heat capacity. Mantle transit times are indicated for some experiments and are calculated by

$$\Delta t_{\text{MT}} = \frac{\Delta t \cdot v_{\text{rms},0}}{D} \tag{11}$$

where Δt is the dimensional time period and $v_{\text{rms},0}$ is the characteristic root-mean-square velocity of the mantle.

2.4. Initial Condition 1: Symmetric Subduction

This study does not aim to explain the initiation of subduction. Therefore, ongoing subduction is initially assumed by placing a vertical cold slab underneath the plate. An initial divergent plate boundary is assumed, and the initial boundary layer thickness w_{BL} increases away from this spreading center toward the subduction zone according to the standard $\sqrt{\text{age}}$-law

$$w_{\text{BL}}(x) = w_{\text{BL},0} \cdot \sqrt{\Delta x_{\text{sc}}} \tag{12}$$

where $w_{\text{BL},0}$ is a constant controlling the maximum thickness of the plate, x is the horizontal coordinate, and Δx_{sc} is the distance from the spreading center at any given position x. The radial component of the initial temperature is then related to plate age as $T_z(x) = T_0 \cdot \text{erf}[(1-z)/w_{\text{BL}}(x)]$, with $T_0 = 0.64$ the initial, nondimensional mantle temperature and z the vertical coordinate ranging between 0 at the bottom to 1 at the top boundary. This leads to an initial divergent boundary (due to ridge push) that supports slab sinking at the beginning of the experiment. The plate thickness becomes self-determined by the model after one complete recycling of this initial cold thermal boundary layer. Its initial value is chosen to be $0.06D$ based on the observation that this is a typical boundary layer thickness with the chosen $Ra = 10^6$ and $H = 20$.

This symmetric initial setup is chosen in order to not bias the experiments toward single-sided subduction (although to avoid perfect symmetry, a small random temperature perturbation of ($\pm$125 K) is applied everywhere except in the sticky air layer). Here it is recognized that a suitable initial setup for a model designed for the understanding of a dynamical process does not necessarily need to be an exact copy of what we see in nature, but it does have to allow (but not prescribe) evolution into the observed state, as well as having a minimal influence on later stages of the simulation.

2.4.1. Initial Slab Depth

The key quantity in this setup is the initial slab depth (d_{slab}). This is varied and tested as explained in detail in the supporting information Figure S2. In order to also give strong plates a chance to initiate subduction, an initial slab depth of $d_{\text{slab}} = 0.5$ is chosen for the experiments presented in this study.

2.5. Initial Condition 2: Ongoing Asymmetric Subduction

In order to investigate the influence of different model parameters, a second initial condition is used. It is a snapshot of a simulation ("standard") that has already developed stable single-sided subduction (see the supporting information Figure S3). In experiments using this initial condition, the convergence velocity of the overriding plate and the subducting plate is often examined. This plate convergence velocity is calculated by summing the plates' horizontal velocities at two points inside the rigid core of each plate. The two points are located at $z = 22$ km depth and at $x = 1156$ km (for the overriding plate) and at $x = 4335$ km width (for the subducting plate) of the domain. The plates behave quite rigidly (i.e., they do not deform significantly), which makes this measurement at only one location meaningful.

3. Results and Discussion

3.1. Double- Versus Single-Sided Subduction

We first reproduce the results of *Crameri et al.* [2012a]. A free-slip surface boundary condition leads to double-sided subduction (Figure 1a), whereas a free surface allows for periods of single-sided subduction (Figure 1b). Adding a weak lubricating layer between the two colliding plates increases the temporal stability of the single-sidedness (Figure 1c). A weak lubricating layer without the free surface, however, is not sufficient to produce single-sided subduction self-consistently (for more details see section 3.4.2). In order to better understand these results, we now examine other aspects of these models.

3.1.1. Stress Distribution

Figures 2a, 2c, and 2e show the stress distribution (i.e., the second invariant of the deviatoric stress tensor) for a free-slip case, a free surface case, and a case with a weak, hydrated crustal layer in addition to a free surface. In the free-slip case, stress is high inside the slab, except near the surface where stress is limited by the friction coefficient and rapid deformation takes place. In the horizontal lithosphere, there are regions of high stress on both sides of the subduction zone, where the plates begin to bend by about 90° over a very short distance (Figure 2a). The slab subsequently sinks nearly vertically into the mantle until it is deflected by the core-mantle boundary; this bending causes a characteristic pattern of bending stress.

The free surface models also have high stress inside the subducting slab but also moderate stress in the horizontal part of the subducting plate extending toward the trench (Figures 2c and 2d). There is also a strong difference in the stress pattern in bending portions of the lithosphere: free surface cases tend to have two high-stress bands separated by a low-stress band inside the slab, whereas free-slip cases just have roughly homogeneous stress inside the slab at shallow depths. This pattern of stress due to bending is characterized by stress accumulations in the top and the bottom part of the deforming plate, because the top part is under extension while the bottom part is under compression. An approximately horizontal, stress-free band ("neutral line") divides these two high-stress areas. The bending stress pattern at the subduction zone has a longer wavelength in the free surface models and the longest when applying a weak crustal layer.

The highest stresses occur in downgoing plate portions and are caused by bending of the high-viscosity slab, the high viscosity being due to strongly temperature-dependent viscosity combined with the "friction coefficient" type yield stress, which is not reached under high confining pressure. The two sharp phase transitions bracketing the upper mantle transition zone are not included here but might lead to a more heterogeneous bending of the slab and a patch of high-stress accumulation just above the transition zone [see, e.g., *Čížková et al.*, 2007]. Furthermore, grain size reduction due to these phase transitions might lead to weakening of the slab [*Karato et al.*, 1980].

The accumulation of weak hydrated crustal material leads to an easily deformable accretionary wedge in which significant stress cannot build up. This wedge and connected layer of weak crust above the subducted slab thus form a low-stress zone (Figure 2e).

Deformation in these models occurs either by plastic failure or diffusion creep. Diffusion creep might be the dominant deformation mechanism in the cold core of sinking slabs only within areas of decreased grain size [*Riedel and Karato*, 1997]. Other deformation mechanisms that might be important in subduction zones are particularly dislocation creep and Peierl's creep [*Čížková et al.*, 2007; *Duretz et al.*, 2011; *Garel et al.*, 2014], which would have the effect of reducing the stress. Even so, in the single-sided models presented here the stress distribution inside the slab (Figures 2c and 2e) shows a clear bending stress pattern, which is consistent with the observation of double seismic zones in nature. A double seismic zone is characterized by two separated lines of enhanced seismic activity along the slab, one at the top and one in the lower part of the slab. Such double seismic zones are generally attributed to the unbending of the slab and are located at positions where the slab descends at around 45° [*Samowitz and Forsyth*, 1981].

The slab dip at the base of the convergence zone for these single-sided subduction experiments is typically around 45°. The single-sided nature of subduction makes this dip more realistic than in free-slip surface models, in which the double-sided subduction leads to near-vertical dip. A weak lubrication layer between the two converging plates further decreases the slab dip toward a shallower lying slab (Figure 1). The dip angle is, thereby, believed to be mainly controlled by the poloidal corner flow induced by the sinking of the slab [*Stevenson and Turner*, 1977]; the lifting force on the slab induced by this corner flow might be slightly overestimated due to the 2-D model setup [e.g., *Dvorkin et al.*, 1993].

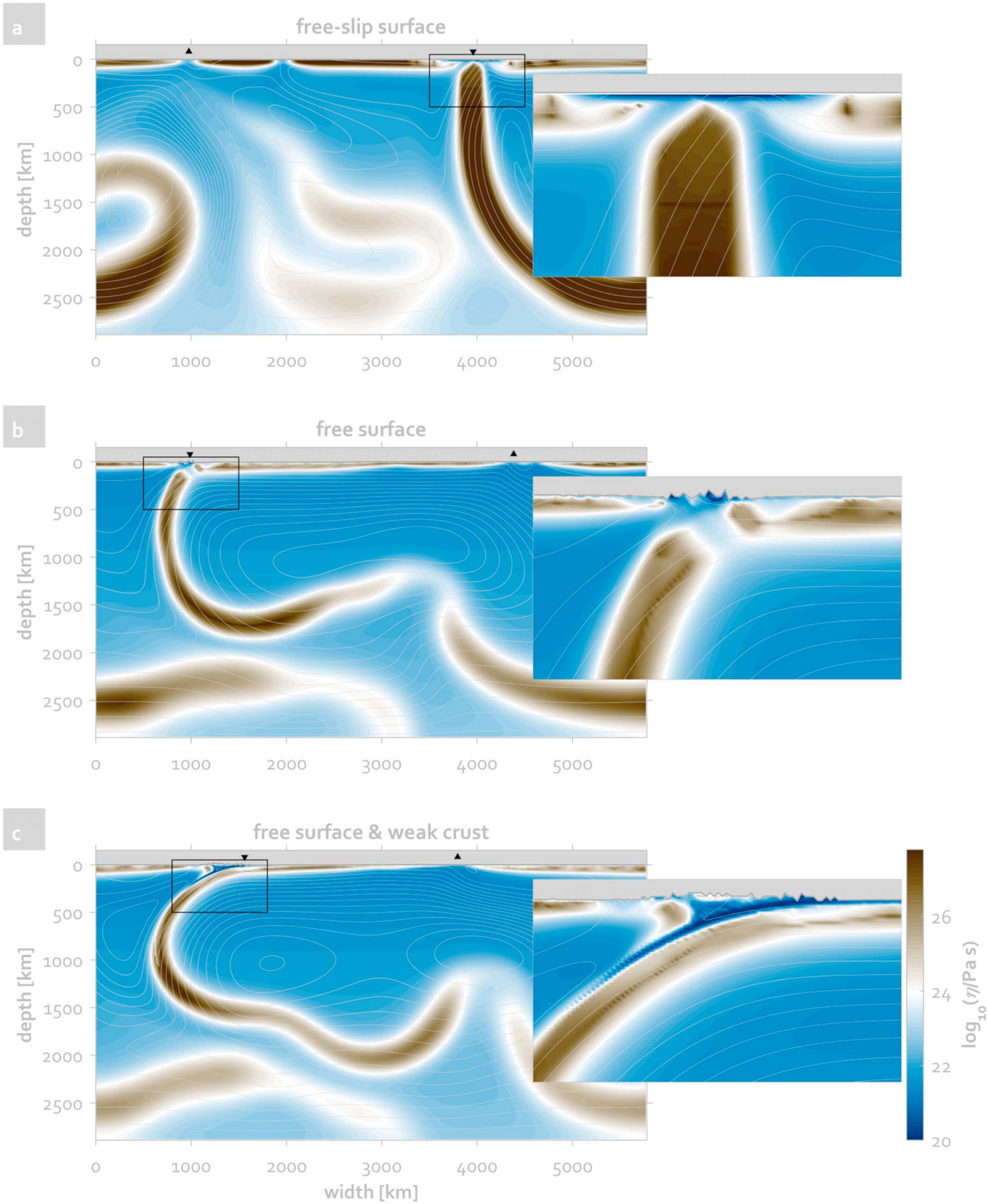

Figure 1. Viscosity field of experiments using different top boundary conditions: (a) free-slip surface (“topBC1”), (b) free surface (“topBC2”), and (c) free surface together with a weak crustal layer (“topBC3”). The grey contours indicate instantaneous streamlines. The sticky air layer in Figures 1b and 1c is visually removed for a better comparison.

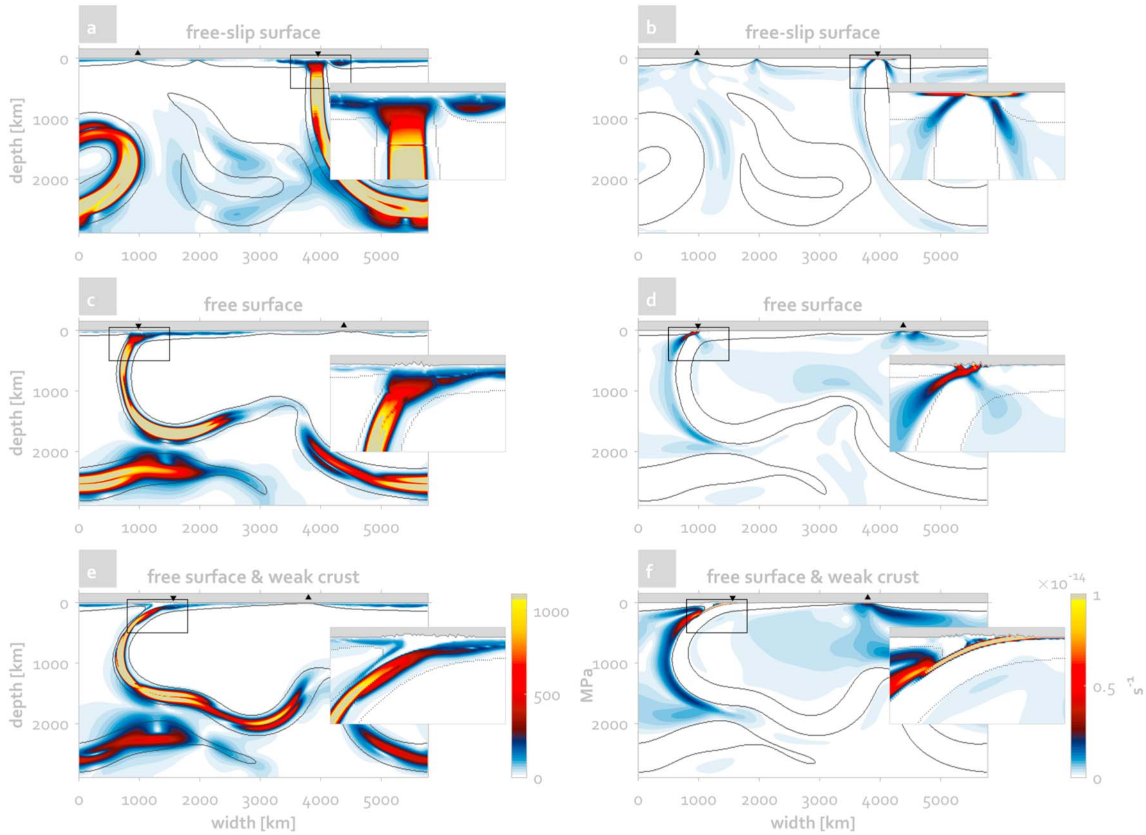

Figure 2. Stress field, i.e., second invariant of stress tensor (left column) and strain rate field (right column) of experiments using different top boundary conditions: (a, b) free-slip surface ("topBC1"), (c, d) free surface ("topBC2"), and (e, f) free surface together with a weak crustal layer ("topBC3"). The black line outlines the cold portions of the model, and the sticky air layer in Figures 2c–2f is visually removed for a better comparison.

Numerical models often impose surface plate motions [e.g., *Bunge et al.*, 2002; *Steinberger et al.*, 2004]. This can, however, lead to unrealistic deformation of the sinking portions of the plate and thus also of the surrounding mantle. The models presented here prevent the introduction of additional energy into the system by being dynamically self-consistent and accounting for the global dynamics of mantle convection.

3.1.2. Strain Rate Distribution

Interplate strain rates at the subduction zone are lower with a free-slip boundary than with a free surface (Figures 2b, 2d, and 2f). With a free-slip boundary (Figure 2b) large strain rates are localized at and below the surface boundary above the downwelling. This is because the downwelling causes a strong under-pressure at the surface since the plate is not free to bend downward, resulting in what would in the absence of yielding be extremely high stresses in a horizontal layer at the top of the lid. The stress distribution in the lid was described by *Fowler* [1985] and further studied by *Solomatov* [2004] with the help of a numerical model. The occurrence of high strain rate at the free-slip boundary is explained by the gigantic normal stress that would be acting there if brittle failure (yielding) did not occur. This gigantic normal stress is formed by maintaining the horizontal balance between the horizontally acting force created by the convective shear stress and the vertically acting force created by the resulting normal stress at the vertical boundary (i.e., the place where the plate cannot move horizontally any further). The (brittle) yield stress limit is therefore easily reached in this zone, and the material fails, becomes weak, and flows effortlessly.

Other prominent zones of high strain rate are observed where both colliding plates are forced to bend strongly to subsequently subduct. This double-pattern shear zone is only weakly present in the free surface case (Figure 2d) and fully absent after the addition of a weak lubricating layer (Figure 2f). The general strain rate pattern in the latter two cases is similar and differs strongly from the free-slip model: The colliding plates do not merge and hence allow for a single strongly localized shear zone. The difference between the two models with a free surface is due to the weak hydrated crust: this weak crust enables a strongly sheared subduction channel below a deeper accretionary wedge.

10.1002/2014JB011664

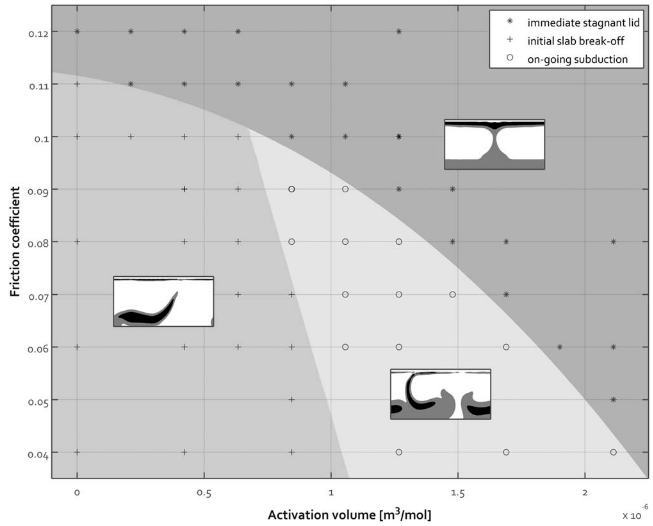

Figure 3. Regime diagram from *Crameri et al.* [2012a] showing the plate tectonic style depending on plate strength (defined by the friction coefficient μ) and viscosity increase with depth (defined by the activation volume V_{act}) resulting in either an immediate stagnant lid, an initial slab break-off, or ongoing subduction.

3.1.3. Flow Velocity and Pattern

Faster root-mean-square (RMS) plate velocities are obtained in the free surface models: single-sided subduction increases average plate speed to around twice that observed with double-sided subduction. At the same slab-sinking velocity, subduction consumes lithosphere twice as rapidly when it is double-sided instead of single-sided, making convective cooling twice as efficient. To equalize the time-averaged heat loss to the internal heating rate, which does not differ between models, the slab-sinking velocity and thus also the subducting plate velocity must be twice as high for single-sided subduction as for double-sided subduction. This leads to equal, model-wide averaged, plate velocities in both models. Additional effects that account for the reduced average plate speed in free-slip cases may be the strong bending of both plates at the trench and the bending and piling up of the double-thickness slab in the deep mantle.

The largest vertical velocities are those of the sinking, subducted plate, which is the main source of buoyancy in the system and hence the main driver of the flow. The plate velocities are closely related to this, and the large-scale velocity field clearly reflects the motions of the sinking slab and plates (Figure 1).

In models with a free surface developing single-sided subduction the flow pattern consists of two major cells: (a) The biggest cell is caused by coupling of shallow mantle material to the direction of movement of the subducting plate, subsequent downwelling, and return flow. In these models—without bottom heating—the upwellings are mainly induced by the movement of the slab remnants close to the core-mantle boundary (CMB) and thus widely distributed. (b) A secondary convection cell is formed in the mantle wedge where mantle material is dragged down with the slab and replaced by the return flow at shallow depth. This cell is able to produce lithospheric extension close to the trench and can lead to behind-arc spreading as originally proposed by *Toksöz and Hsui* [1978]. In the case of double-sided subduction, the major upwelling is located far away from the major downwelling (i.e., the sinking slab) reflecting the symmetry produced by double-sided subduction.

3.2. Obtaining Ongoing Subduction

In some cases long-lived subduction is obtained, but this depends strongly on some key parameters. Following *Crameri et al.* [2012a], three different regimes can be found when varying two key parameters over a limited range of values. These two parameters are (a) the strength of the plate, as controlled by the friction coefficient, and (b) the viscosity increase with depth in the mantle (Figure 3). The time evolutions of such experiments representing the three different regimes are shown in Figure 4.

Figures 4a–4c show the difference between experiments with different plate strength controlled by the friction coefficient ($0.07 < \mu < 0.11$). Figures 4d–4f show results after applying different viscosity increases with depth, controlled by activation volume ($2.0 < V_{act} < 6.0$). Varying either parameter can cause a transition

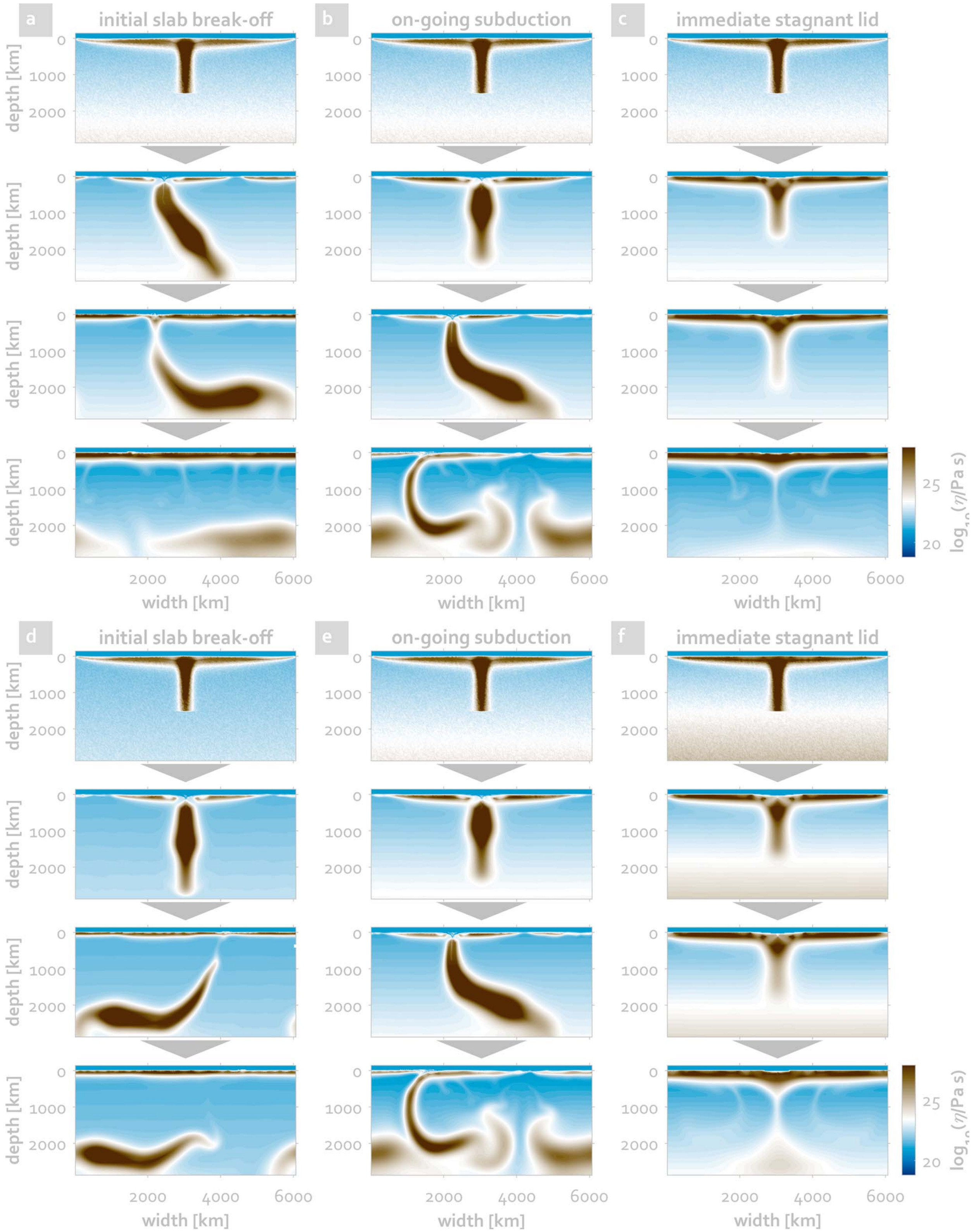

Figure 4. Time evolution of numerical experiments with $V_{act} = 4.0$ and with variable plate strength ("regime1"). Shown is the viscosity field at different time steps for friction coefficients of (a) $\mu = 0.07$, (b) $\mu = 0.09$, and (c) $\mu = 0.11$. Below is the time evolution of numerical experiments with $\mu = 0.09$ and variable viscosity increase with depth ("regime2"). Shown is the viscosity field at different time steps for (d) $V_{act} = 2.0$, (e) $V_{act} = 4.0$, and (f) $V_{act} = 6.0$. Both types of experiments result in three different regimes identified as (Figures 4a and 4d) initial slab break-off, (Figures 4b and 4e) ongoing subduction, and (Figures 4c and 4f) an immediate stagnant lid (see Figure 3).

to another of the three regimes of subduction behavior. The immediate stagnant lid regime is obtained with a strong plate and/or a large viscosity increase with depth, because the stiff/normal plate does not fail when subjected to a normal/low slab pull. On the contrary, the rapid slab break-off regime is obtained with a weak plate or, similarly, a small viscosity increase with depth, because the weak/normal plate fails to transmit the normal/strong slab pull. The ongoing subduction regime is obtained when the slab pull (controlled by the viscosity increase with depth) is sufficient to break the plate and yet low enough to be entirely transmitted to the surface. In this case, the initial symmetrical subduction setup evolves either by remaining symmetric (and double-sided) when having a free-slip surface (Figure 1a) or evolves by developing asymmetric (and single-sided) subduction (with intermediate periods of double-sided subduction) when having a free surface (Figure 1b).

The boundary separating initial slab break-off and ongoing subduction is shifted slightly to the left (i.e., to lower friction coefficient and/or lower activation volume) when using higher resolution models. This is caused by better resolution of the subducting plate and its strong core, which can be lost at low resolution and thus facilitate slab break-off (see supporting information Figure S1).

3.3. Dynamical Behavior of Ongoing Subduction

Ongoing subduction in these experiments is characterized by dynamically distinct phases. Typically, the rate of subduction is similar to the rate of spreading, so that the subducting plate remains the same size. Still, there are time periods when the subducting plate is consumed faster than it is produced; the spreading center therefore migrates toward the subduction zone and can influence the dynamics there.

In the two-dimensional experiments presented here, the single-sidedness of subduction is not a perfectly temporally stable feature. Rather, single-sided subduction is regularly interrupted by intermediate phases of symmetric, double-sided subduction or even shutdown early on. During double-sided subduction, weak portions of the overriding plate (e.g., a spreading ridge) can return the system into single-sidedness, whereas both a young subducting plate and an old overriding plate can turn the system into double-sidedness. This behavior is illustrated in the supporting information Movie S1,where single-sided subduction occurs during $\Delta t_{MT} = 2.4$ mantle transit times. Single-sided subduction is more temporally stable in models with a larger aspect ratio or in a 3-D shell [see *Crameri and Tackley*, 2014]. The time periods of self-consistent single-sided subduction obtained with the models presented here are, nevertheless, sufficient to study the effects of various physical complexities on 2-D subduction dynamics.

The surface thermal boundary layer is usually divided into more than one plate, while (for the aspect ratio used here) there is only one plate being subducted. This results in one nonsubducting plate that becomes progressively older, colder, and thicker, until it starts to subduct itself, leading to an abrupt change in the overall dynamics of the model. Such dynamical behavior of a mobile lid is observed and described in the following sections.

3.3.1. Subduction Polarity Reversal

Asymmetric single-sided subduction is characterized by a strong, negatively buoyant subducting plate underthrusting an upper plate. If the subducting plate becomes less negatively buoyant (e.g., younger) at the trench and the upper plate happens to grow thicker and more negatively buoyant (e.g., older), it can lead to a subduction polarity reversal as shown in Figure 5 and in the supporting information Movie S1. This process is characterized by an upper plate that cools down sufficiently and hence becomes thick and heavy while the converging subducting plate becomes younger and thinner, hotter and less negatively buoyant. This enables the upper plate to start sinking under its own weight at the subduction zone. After an intermediate very short period of double-sided subduction, the former overriding plate gains control at the subduction zone due to its greater negative buoyancy and develops single-sided subduction in the opposite direction to that previously. In the limited space provided by the simple 2-D Cartesian model domain, subduction polarity reversals are often the only possibility for the evolving system to prevent early subduction termination and a stagnant lid regime.

3.3.2. Subduction Shut-Off

There are two main reasons for subduction to shut off in the models presented here. They have in common that the resisting forces of subduction (i.e., viscous coupling between the subducting plate and its surroundings (including the overriding plate) and plate bending) become stronger than the forces driving subduction (i.e., negative buoyancy of the subducting plate and ridge push).

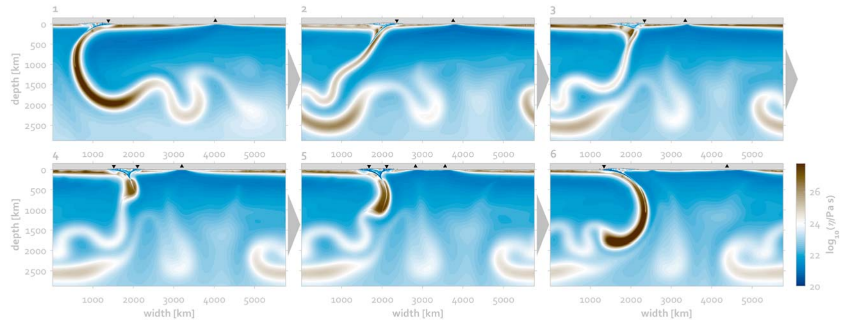

Figure 5. Time evolution showing subduction polarity reversal (left to right) of experiment "comp" at (top) $t_1 = 3.08$ Ga, $t_2 = 3.38$ Ga, and $t_3 = 3.54$ Ga, and (bottom) $t_4 = 3.68$ Ga, $t_5 = 3.7$ Ga, and $t_6 = 3.76$ Ga. The shown time period spans $\Delta t_{MT} = 1.2$ mantle transit times.

The most common reason for downwelling at an ongoing subduction zone to be shut off in our experiments is the approach of a spreading center on the subducting plate (Figures 6a and 6b). Ridge-trench collision has also been studied in other numerical models [*Burkett and Billen*, 2010] and leads to a warmer and thinner and thus less negatively buoyant subducting plate. This slows the downwelling motion, leading to heating and weakening of the subducted plate portion until it finally breaks off, typically at the place where the partially subducted spreading center is (see also the supporting information Movie S1).

Another reason for subduction to shut off is an increase in viscous coupling between the two converging plates, due to the viscosity of the subduction channel rising. The usual reason for this appears to be a reduction of slab pull due to accumulation of slab material in the more viscous lower half of the mantle; the stress thus decreases to levels at which yielding no longer takes place. Once subduction becomes blocked, the slab breaks off and sinks. Another possible reason is a reduction in the thickness of the weak crust lubricating layer in the subduction channel (Figures 6c and 6d). The subducted portion remaining at shallow depth and still connected to the surface plate is removed by small-scale convection and progressive thermal diffusion.

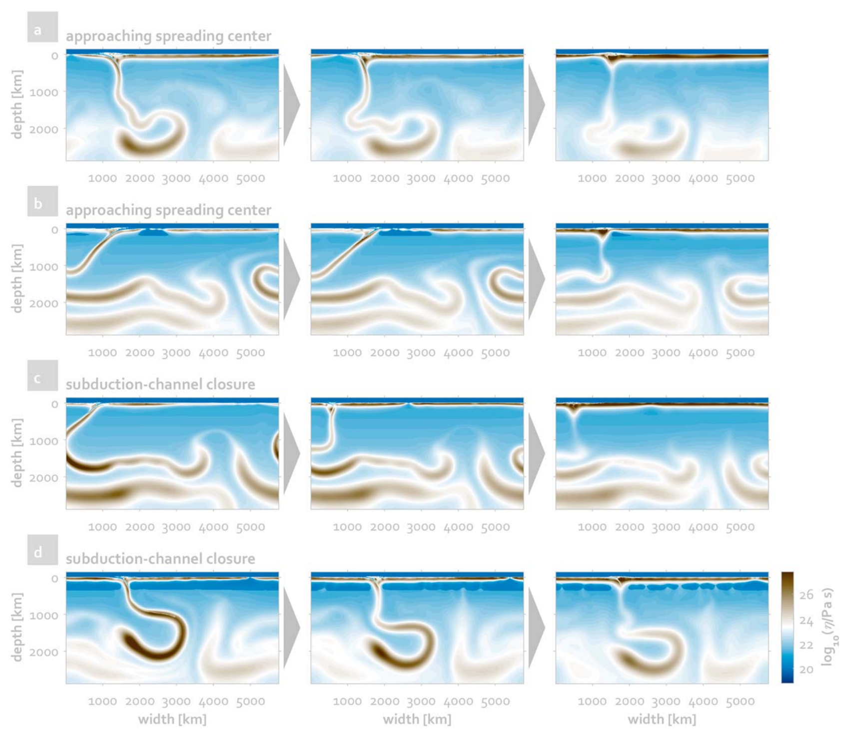

Figure 6. Time evolution (left to right) of subduction shut-off in different experiments showing slab break-off caused by (a, b) an approaching spreading center ("comp" and "standard") or (c, d) the closure of the subduction channel ("comp" and "mvr").

10.1002/2014JB011664

In these two-dimensional models, subduction shut-off by one of the mechanisms discussed above sometimes results in termination of mobile-lid mode and the beginning of a stagnant lid phase.

3.4. Influence of Key Parameters

In this section we systematically evaluate the influence of the values of key parameters and physical complexities.

3.4.1. Friction Coefficient

A strong plate is one necessity for stable single-sided subduction. In our model, the strength of a plate at shallow depth is limited by brittle failure as expressed by the friction coefficient (see equation (6)), which we here vary. Three regimes are found to occur depending on its value:

1. A low friction coefficient (e.g., $\mu < 0.04$) results in a mobile-lid regime with "blob-like" subduction characterized by regular dripping of small plate portions (not shown). The plate is very weak, which makes it difficult for stress to be transferred along it. As a result, the force caused by the negative buoyancy of the slab (i.e., slab pull) causes the subducting plate to fail and finally break off. This process takes place at a very early stage of subduction, and hence only small portions ("blobs") break off and sink into the lower mantle.
2. An intermediate friction coefficient (e.g., $\mu \approx 0.06$) makes the stronger slab capable of transmitting the force of slab pull to the parts of the plate at the surface. This results in ongoing subduction and a more realistic average plate length within the top thermal boundary layer.
3. A too high friction coefficient (e.g., $\mu > 0.11$) prevents the lithosphere from yielding at the stress levels produced by convection. Subduction, which is initiated and maintained by lithosphere-scale failure, does not set in, and the system consequently forms a rigid, stagnant lid.

The threshold values defining the regime boundaries cited above are typical but also depend on the magnitude of the pressure-dependent viscosity increase with depth, which is controlled here by the activation volume [see *Crameri et al.*, 2012a] (see section 3.2). It should be noted that the friction coefficient values needed for ongoing subduction are substantially lower than those measured in laboratory experiments, and this is a common finding of numerical modeling of plate boundaries [*Moresi and Solomatov*, 1998; *Trompert and Hansen*, 1998; *Tackley*, 2000a, 2000b; *Bird*, 2003; *van Heck and Tackley*, 2008; *Foley and Becker*, 2009].

3.4.2. Weak Crustal Layer

Different rock types clearly have different strengths, which is here expressed in terms of diffusion creep viscosity and yield stress. The deformation history and volatile content also play a major role. In a subduction zone setting, a weak subduction channel, consisting of strongly deformed, hydrated crustal rock surrounded by stronger crustal and other rocks, between the two plates probably plays a key role [*Cloos and Shreve*, 1988]. Accounting for this weak layer has been shown to be important for self-sustaining subduction [*Lenardic and Kaula*, 1994] and its asymmetry on regional [*Tagawa et al.*, 2007; *Gerya et al.*, 2008] and global scales [*Crameri et al.*, 2012a].

While periodic shear heating at depths of ~30–50 km [*Kelemen and Hirth*, 2007] and the presence of fluids (CO_2, H_2O) down to 200 km [*Peacock*, 1990; *Schmidt and Poli*, 1998] might cause slip on such a well-established weak shear zone in nature, deformation in such a layer has to be parameterized in a long-term global model like the one presented in this study. Reducing the creep viscosity of the shear zone, its yield strength (expressed either as a constant value or as a friction coefficient), or both can achieve a decreased resistance against deformation. Here we test the different possibilities and investigate their impact on single-sided subduction.

Figure 7 shows a comparison of experiments with different rheological descriptions of the weak hydrated crust. The weakening is described by either (a) a viscosity and a yield stress reduction by a factor of 100 (Figure 7a), (b) a viscosity reduction by factor of 10 and a very low, depth-independent yield stress (Figure 7b), or (c) solely a low, depth-independent yield stress (Figure 7c). In all models the viscosity variation is restricted to 9 orders of magnitude and the yield strength contains a term for cohesion (see equation (6)). This thus sets a minimum value that can be reached by any kind of weak layer.

A factor of 100 reduction of both the viscosity and friction coefficient of the crust results in strong accumulation of crust at the collision zone, producing a large accretionary prism and a deep trench (Figure 7a), but the subduction channel is somewhat entrained by the slab and does not perfectly decouple the two plates.

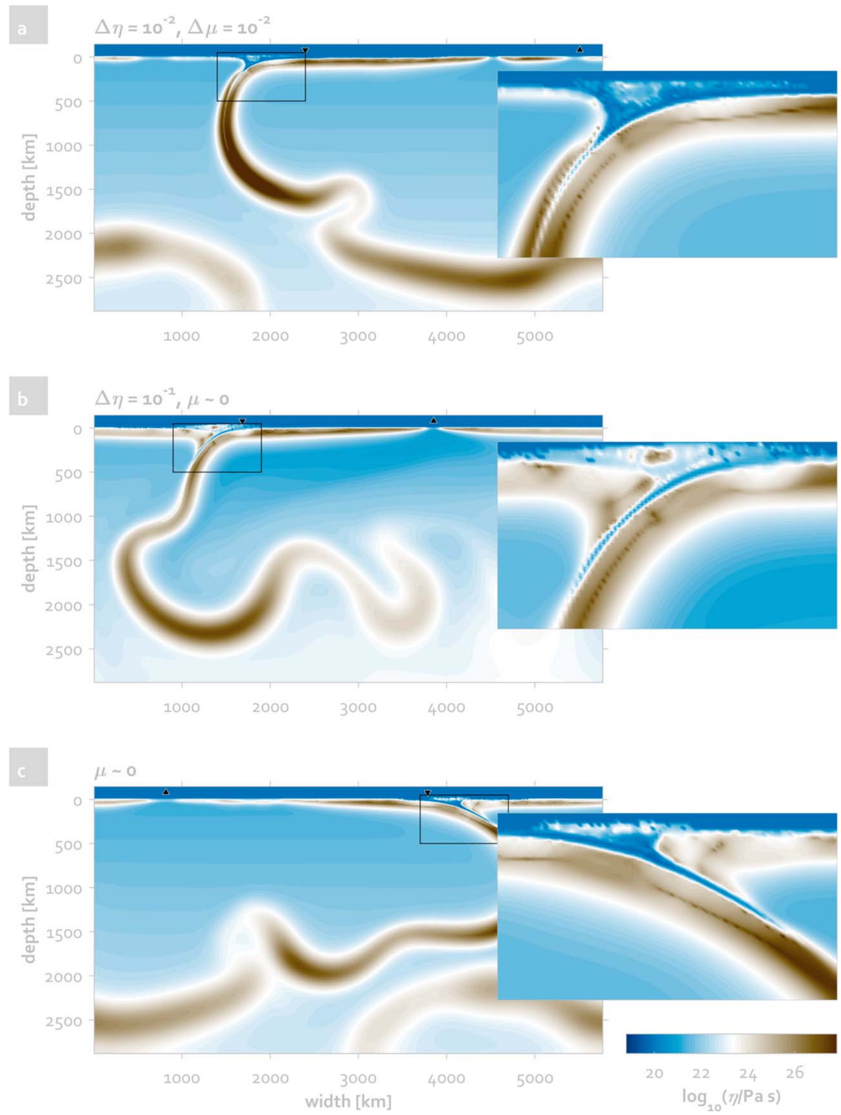

Figure 7. Comparison between experiments (based on "topBC3") with different weak crustal layer description showing cases with crustal weakening by (a) a viscosity and a yield stress reduction by a factor of 100; (b) a viscosity reduction by a factor of 10 and a very low (C_{crust} = 157.7; μ_{crust} = 0.001), depth-independent yield stress; and (c) only by having a low (C_{crust} = 157.7; μ_{crust} = 0.001), depth-independent yield stress.

Better results are obtained by setting the crustal friction coefficient close to zero so that the weak crustal layer has a very low, almost constant yield stress (Figure 7b); then a very good decoupling of the two plates is observed. Fully disabling the prescribed effective viscosity decrease of the weak hydrated crust and instead relying solely on the depth-independent yield stress for weakening the crust (Figure 7c) brings further improvement. Most of the experiments presented in this manuscript therefore use this third description of a weak hydrated crustal layer.

A weak crustal layer has been shown to decouple the plate from the free-slip surface, which allows imposed single-sided subduction to remain single-sided over short time periods [*Quinquis et al.*, 2011]. Yet we here show that a weak crustal layer is insufficient on its own (i.e., without a free surface) to produce single-sided subduction self-consistently, unless single-sidedness is imposed initially: Figure 8 shows model evolution for a free-slip case with a weak lubricating layer as used in the model shown in Figure 7c. Although subduction becomes asymmetric, it always remains double-sided. Even during phases with ridge-trench collisions (the most favorable setting for free surface models to switch to single-sided subduction), the downwelling remains double-sided.

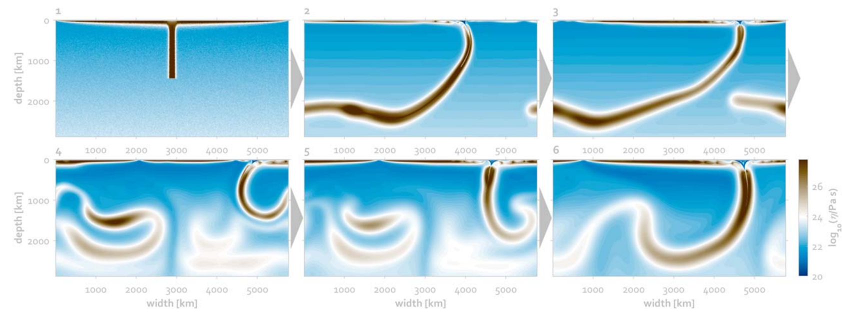

Figure 8. Time evolution of experiment "topBC4" with a vertically fixed, free-slip surface plus a weak lubricating layer. Even over long time periods, subduction never becomes single-sided.

A weak lubricating layer brings subduction in a free-slip model somewhat closer to single-sidedness as the weak layer mimics the effect of a sticky air layer: It allows the plate (i.e., the strong plate core) to bend more naturally (i.e., less abruptly) by building up a viscous foreland bulge and a deep trench. However, there is still significantly more work involved to deform the weak crustal layer as compared to a sticky air: The weak crustal layer is too viscous and too thin to properly decouple the strong plate core from the fixed top boundary of the model [*Crameri et al.*, 2012b].

3.4.3. Viscosity Contrast

The rate of viscosity variation with temperature defined by E_{act} (see equation (5)) is important for the model evolution; we thus here test three different values, the highest of which is closest to a laboratory-measured value (Figure 9a). A large viscosity contrast between cold, stiff plates and hot, weak mantle leads to a stronger decoupling between them (i.e., between hot and cold parts of the model) and localizes the convective cells as is illustrated by Figure 9: The streamlines in the experiment with the high viscosity contrast shown in Figure 9a become narrower and shallower than the streamlines of the experiments with lower viscosity contrasts shown in Figures 9b and 9c, which indicates a stronger and shallower flow cell.

Subduction velocities and trench retreat velocities are generally much smaller for a lower viscosity contrast in the models presented here (Figure 10a). The primary reason for this is that the viscosity of the ambient mantle is higher in these cases (Figures 9b and 9c), so slab-sinking rates are lower. The relative weakness of

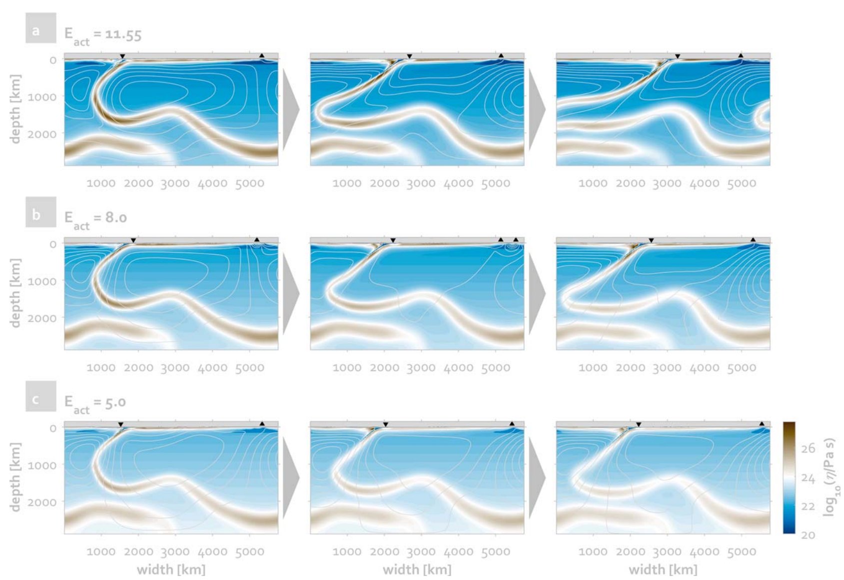

Figure 9. Time evolution (from left to right) of experiments based on "standard" with different viscosity contrast shown for (a) $E_{act} = 11.55$, (b) $E_{act} = 8.0$, and (c) $E_{act} = 5.0$. Grey contours represent streamlines. Simulations are started from the same, well-developed initial condition that was run using $E_{act} = 11.55$. Times are 4 Ma (left), 80 Ma (middle), and 160 Ma (right).

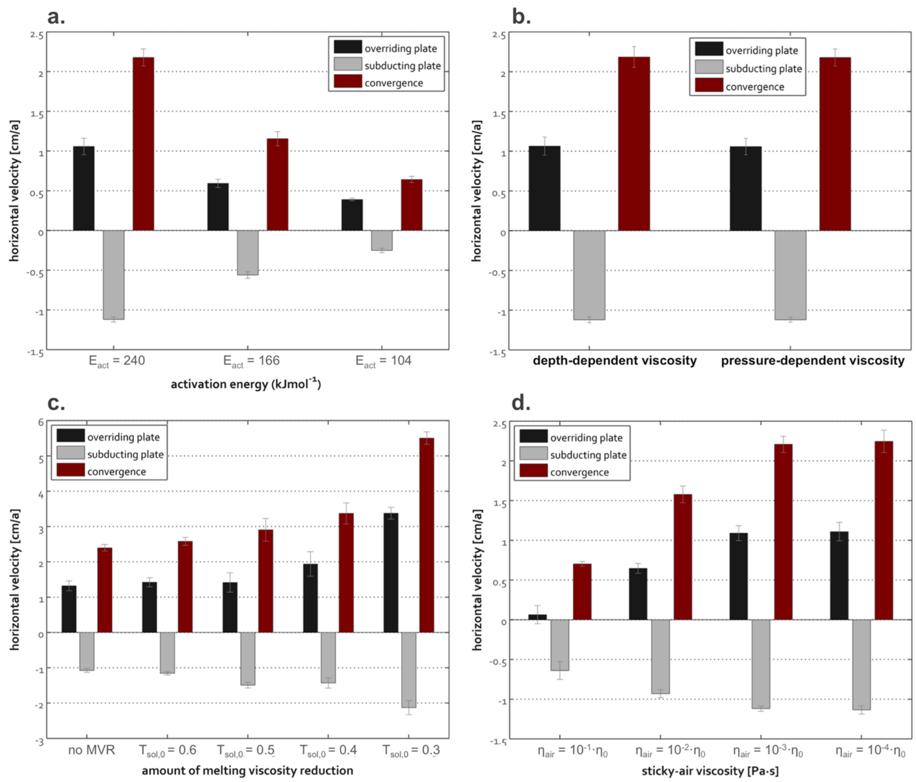

Figure 10. Mean horizontal velocity shown for the overriding plate/trench (black), the subducting plate (grey), and their convergence (red). (a) An experiment with different viscosity contrasts controlled by E_{act} from high viscosity contrast (left-hand side group) to low viscosity contrast (right-hand side group), corresponding to cases shown in Figure 9. (b) An experiment with depth-dependent (left-hand side group) versus pressure-dependent viscosity (right-hand side group). (c) An experiment with different sized asthenospheres arising from melting viscosity reduction, ranging from a case without MVR defined by $T_{sol,0} = \infty$ (left-hand side) to cases with more MVR that is varied between MVR only at spreading centers ($T_{sol,0} = 0.6$), up to a very thick MVR layer ($T_{sol,0} = 0.3$, right-hand side). (d) An experiment with different sticky air viscosity, whereby values are given with respect to the characteristic viscosity η_0 and are (left to right) on the order of $10^{-1}\eta_0$ Pa s, $10^{-2}\eta_0$ Pa s, $10^{-3}\eta_0$ Pa s, and $10^{-4}\eta_0$ Pa s. The mean is taken over a time period of (Figures 10a and 10b) 100 Ma, (Figure 10c) 25 Ma, or (Figure 10d) 80 Ma corresponding to approximately $\Delta t_{MT} = 0.4$, 0.1, and 0.3 mantle transit times, respectively. The standard deviation is indicated by grey error bars.

the slab and surface plates also leads to them behaving less as a single entity, i.e., less transmission of stress and more internal deformation.

A higher viscosity contrast tends to favor single-sided subduction for the same reason as mentioned above: Deformation is more localized and thus allows for a narrow subduction fault that prevents strong viscous coupling between the two colliding plates.

However, in experiments employing a high viscosity contrast (e.g., "standard") subduction initiation is found to be difficult once a stagnant lid has formed. Subduction often does not reinitiate once the model is in the stagnant lid regime. A lower viscosity contrast, as has been used in many other mantle convection models with yielding-induced plate tectonics containing double-sided subduction [e.g., *Tackley*, 2000a, 2000b; *van Heck and Tackley*, 2008; *Rolf and Tackley*, 2011] appears to allow subduction to restart more readily, although this needs to be carefully tested in future studies.

The effective viscosity ratio between slab and surrounding mantle on Earth is believed to be around 1–7 $\times 10^2$, a value that is determined from analogue and numerical modeling of subduction zone geoid [*Moresi and Gurnis*, 1996], slab strain rates [*Billen et al.*, 2003], slab bending resistance [*Wu et al.*, 2008; *Stegman et al.*, 2010], slab and trench geometries [*Schellart*, 2008b], minimum curvature radii of subducted slabs [*Ribe*, 2010], global trench migration velocities [*Schellart*, 2008a], and subduction partitioning (i.e., the ratio between plate velocity and trench migration velocity) [*Funiciello et al.*, 2008]. This viscosity contrast is much lower than the contrast that would be calculated from equation (5) using laboratory values of

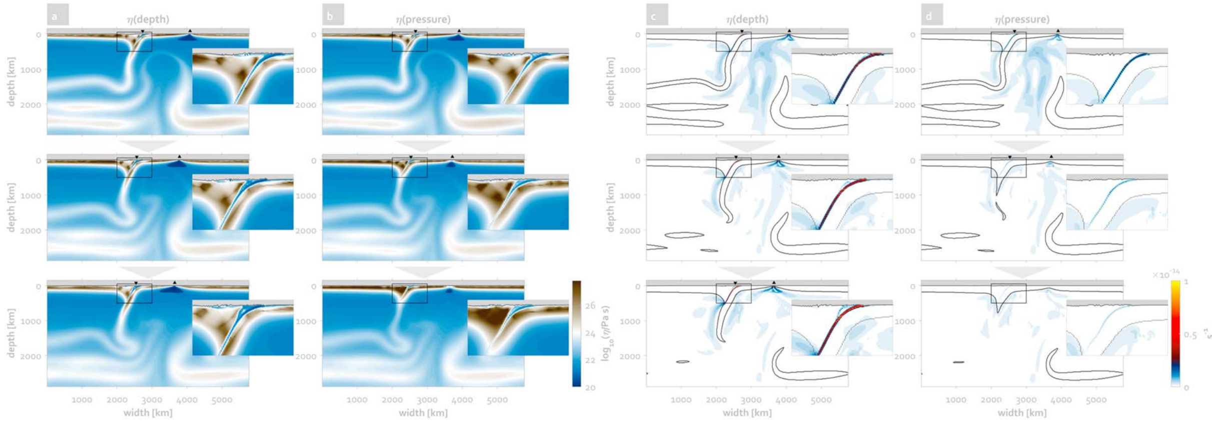

Figure 11. Comparison between time evolutions of experiments based on "standard" calculated with (a, c) a depth-dependent and (b, d) a pressure-dependent viscosity shown for (Figures 11a and 11b) effective viscosity and (Figures 11c and 11d) strain rate. Black contours outline the cold portions of the model.

activation energy before yielding is taken into account. A reconciliation is that the above observation-based studies are determining an effective viscosity, i.e., taking into account plasticity and other nonlinear creep behaviors and not the diffusion creep viscosity as expressed in equation (5). Indeed, in our presented models the effective viscosity contrast between the bending part of the slab and the surrounding mantle does seem to be in the range of 2 to 3 orders of magnitude, i.e., from about 10^{22} Pa s in the general mantle to 10^{24}–10^{25} Pa s in the bending part of the slab (see Figure 9a).

3.4.4. Hydrostatic Versus Total Pressure

Physically, the pressure appearing in equations (5) and (6) is the total pressure (i.e., including dynamic pressure), whereas what is typically used in geodynamic modeling codes is the hydrostatic pressure calculated simply from the depth. In regions of high stress there may be a significant difference between the two, for example, in the top part of a subducting slab that is under extension. Thus, we here test whether the dynamic pressure makes a difference in the current models (Figure 10b). Overall, the difference is small.

Small differences in calculated effective viscosity can nonetheless lead to important differences in overall behavior. Figure 11 shows a critical state in two experiments, one with depth-dependent and the other with pressure-dependent viscosity, shortly after beginning the simulation from the same initial condition. A thick subduction zone develops, and the negative buoyancy of the subducting plate becomes critical to maintain subduction. As the downwelling motion slows down, the experiment with depth-dependent viscosity is able to maintain the weak subduction channel, whereas the pressure-dependent viscosity case is not (Figures 11c and 11d). In the latter case, subduction therefore shuts down, whereas subduction continues in the first case.

3.4.5. Presence of a Weak Asthenosphere

A weak asthenosphere is typically thought to help in promoting a mobile-lid style of plate tectonics [*Zhong and Gurnis*, 1996; *Zhong et al.*, 1998; *Richards et al.*, 2001; *Höink et al.*, 2012]. The use of a viscosity that is temperature-dependent and increases with depth, as used in all cases in this study, does give a viscosity minimum below the lithosphere, which can be considered to be a weak, gradual asthenosphere (see, e.g., section 2). To produce a more pronounced and localized asthenosphere, we also apply the "melting viscosity reduction" (MVR) criterion from [*Tackley*, 2000b]. In this, the viscosity is reduced by a factor of 10 in regions where the temperature exceeds a simple linear solidus expressed nondimensionally as

$$T_{\mathrm{sol}} = T_{\mathrm{sol},0} + 2\,(1 - z) \tag{13}$$

where the vertical coordinate z is 0 at the CMB and 1 at top boundary. $T_{\mathrm{sol},0}$ is the surface solidus temperature and is varied to give differently sized low-viscosity regions. When $T_{\mathrm{sol},0}$ is high (e.g., nondimensional 0.6, corresponding to 1800 K), only small regions below spreading centers (with upwelling flow) have the lowered viscosity, whereas when $T_{\mathrm{sol},0}$ is low (e.g., nondimensional 0.4, corresponding to 1300 K), a low-viscosity channel extends laterally all the way below the lithosphere except in regions of cold downwellings.

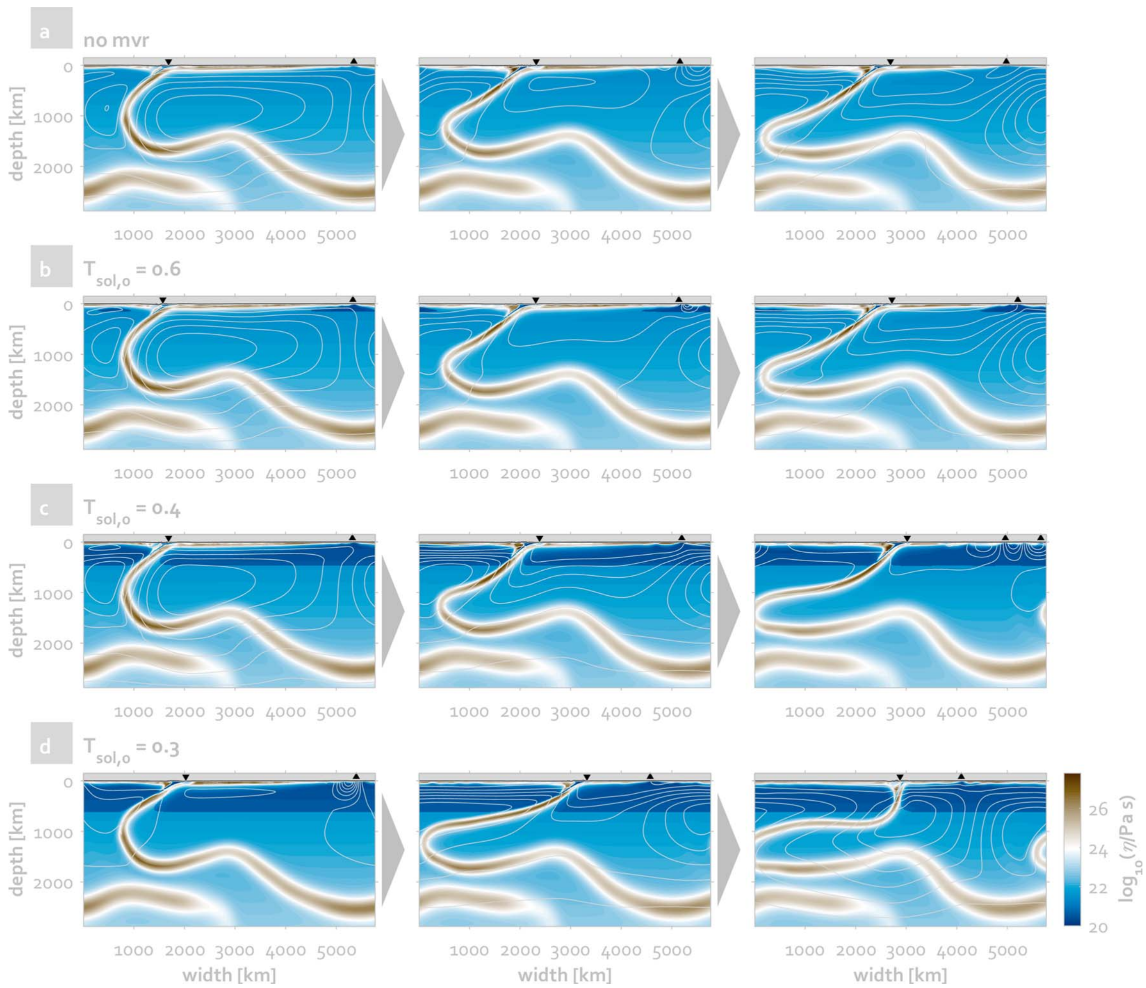

Figure 12. Effects of a low-viscosity asthenosphere introduced using the melting viscosity reduction (MVR) criterion: Comparison between the time evolutions of experiments based on "standard" (a) without MVR, (b) including a thin layer of MVR with $T_{\text{sol},0} = 0.6$, (c) with an intermediate layer of MVR with $T_{\text{sol},0} = 0.4$, and (d) with a thick layer of MVR defined by $T_{\text{sol},0} = 0.3$. Snapshots are taken at 4 Ma (left column), 42 Ma (middle column), and 85 Ma (right column), and grey streamlines indicate mantle flow.

Adding this MVR asthenosphere to the models presented in this study has a significant effect on their dynamic evolution (Figure 12). A limited asthenosphere below spreading centers makes them more localized but does not contribute to significantly faster plate movement. In contrast, a weak asthenosphere with global extent results in substantially faster plate velocities. The time-averaged convergence of the two adjacent plates is fastest in the model employing the lowest solidus (i.e., having the thickest asthenosphere) as shown in Figure 10c. The movement of the subduction trench behaves accordingly and retreats fastest for thicker asthenosphere, as can be seen in Figure 12. Small-scale convection may also be facilitated by the low-viscosity asthenosphere; some small-scale complexity can be seen in the case with $T_{\text{sol},0} = 0.4$. Our general experience is that MVR also makes subduction more stable and longer lasting. In mantle wedges, MVR can be considered as a proxy for fluid and melt, which thus might be an important ingredient for ongoing subduction on a rocky planet. *Höink et al.* [2012] also found that the presence of an asthenosphere makes plate tectonics more likely, although they found that a thinner asthenosphere is more effective at increasing stresses exerted on the plates, something that we do not measure here.

3.4.6. Sticky Air Viscosity

The free surface in the presented models is generated by inserting a sticky air layer in the top section of the numerical domain (see section 2). Here the viscosity of the sticky air is varied in order to check that it is sufficiently low so as not to influence the tectonics and to quantify the effect of a viscosity that is too high (Figure 13). *Crameri et al.* [2012b] provide quantitative criteria for testing the qualities of a sticky air layer.

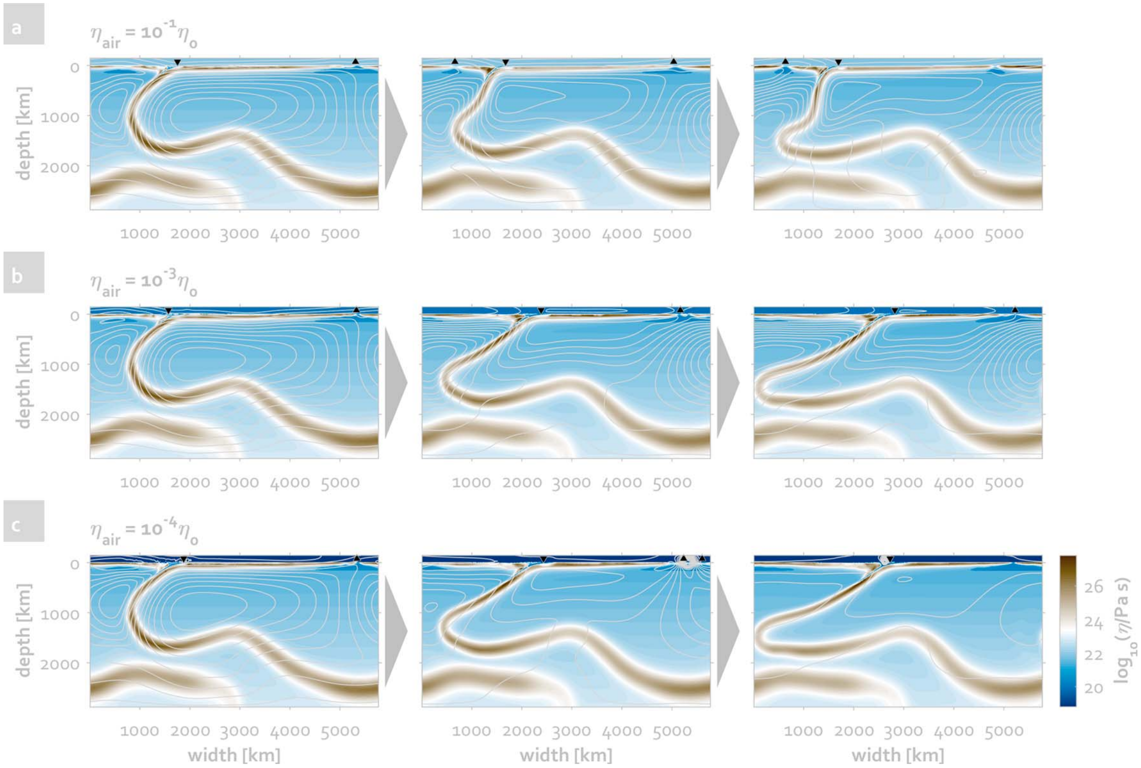

Figure 13. Comparison of subduction behavior between experiments based on "standard" with different sticky air viscosity started from the same initial condition (left column). Shown are different viscosity contrasts between sticky air and the characteristic viscosity of (a) 10^{-1} Pa s, (b) 10^{-3} Pa s, and (c) 10^{-4} Pa s. Time evolution (left to right) is shown at three different moments in time, at 4 Ma (left), 50 Ma (middle), and 97 Ma (right), and grey streamlines indicate mantle flow.

From the three different model-dependent criteria given there (general criterion, isostatic criterion, and Stokes criterion) we choose the Stokes criterion

$$C_{\mathrm{Stokes}} = \frac{1}{16}\frac{\Delta\rho}{\rho}\left(\frac{h_{\mathrm{model}}}{h_{\mathrm{st}}}\right)^3 \frac{\eta_{\mathrm{st}}}{\eta_{\mathrm{ch}}} \tag{14}$$

which indicates traction-free surface movements that are driven by a Stokes process (e.g., a rising plume or a sinking slab) when $C_{\mathrm{Stokes}} \ll 1$. Here $\Delta\rho = 100\ \mathrm{kg\ m^{-3}}$ is the density difference between slab and surrounding mantle, $\rho = 3300\ \mathrm{kg\ m^{-3}}$ is the reference density, $h_{\mathrm{Model}} = 2890$ km is the depth of the mantle, $h_{\mathrm{st}} = 152$ km is the thickness of the sticky air layer, $\eta_{\mathrm{st}} = 7.7 \times 10^{19}$ Pa s is the sticky air viscosity, and $\eta_{\mathrm{ch}} = 7.7 \times 10^{22}$ Pa s is the characteristic viscosity.

A high sticky air viscosity ($\eta_{\mathrm{air}} > 10^{-1}\eta_0$) that has $C_{\mathrm{Stokes}} > 1.3$ exerts significant resistance on movements at the surface boundary, while a low sticky air viscosity ($\eta_{\mathrm{air}} \leq 10^{-3}\eta_0$) with $C_{\mathrm{Stokes}} \leq 0.013$ allows for a free evolution of rock-air boundary displacements. This can be observed in the plate convergence velocities for the different experiments shown in Figure 10d.

A sticky air viscosity of $\eta_{\mathrm{air}} = 10^{-3}\eta_0$ with $C_{\mathrm{Stokes}} = 0.013$ is chosen for the simulations shown in this study because there is no significant difference in comparison to experiments employing lower values but still reasonable computational efficiency.

3.4.7. Modeling Implications and Observational Phenomena

An interesting modeling feature that is observed both in our modeling study and in nature is the occurrence polarity reversals in the subduction direction. Such subduction polarity reversal is observed in nature and was first proposed to be caused by an arc-continent collision [*McKenzie*, 1969]. In this scenario, two oceanic plates converge until a continent on the subducting plate reaches the subduction zone. Continental crust cannot sink and so shuts off the subducting motion of the sinking plate, while the formerly overriding oceanic plate is negatively buoyant and starts to subduct: The direction of underthrusting thus changes. However, the leading edge of an overriding plate in an ocean-ocean subduction setting is likely to be both

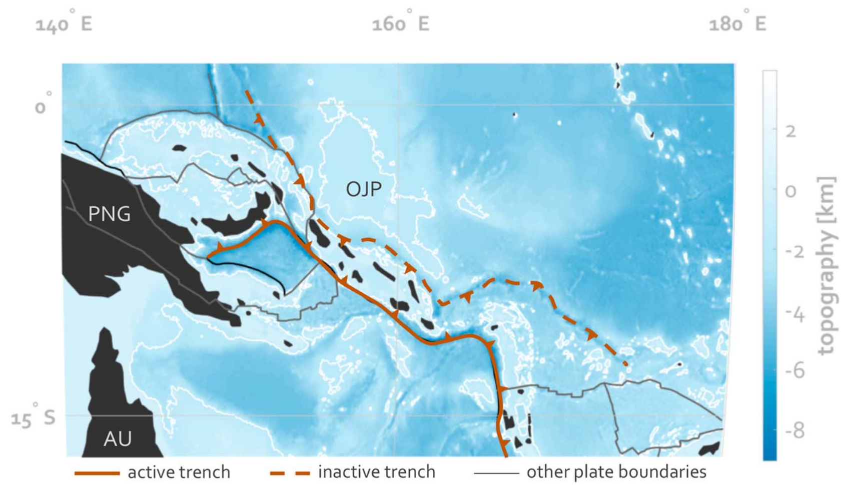

Figure 14. Summary of active and Neogene plate boundaries of Melanesia [after *Taylor and Karner*, 1983; *Cooper and Taylor*, 1985]. Shown is the collision zone between the Indo-Australian Plate (southwest) including Australia (AU) and Papua New Guinea (PNG) and the Pacific Plate (northeast) including the Ontong Java Plateau (OJP). The bluish color indicates seafloor topography from *Smith and Sandwell* [1997]. The white contour indicates 2 km below seafloor.

buoyant and weak due to a light magmatic arc crust and a thin lithospheric mantle. Its buoyancy might inhibit subduction initiation. Its weakness, however, might lead to horizontal shortening and thus thickening of the thin lithospheric mantle during the reorganization previous to the polarity reversal, which finally (due to the increased buoyancy) would again allow the overriding plate to subduct.

The first direct seismic evidence of a reversal in subduction polarity at an island arc was presented by *Cooper and Taylor* [1985]. They revealed the existence of two juxtaposed Wadati-Benioff zones of opposite polarity below the Solomon Island arc: The northeast dipping zone is associated with the active sinking of the Indo-Australian plate and the southwest dipping zone with the inactive North Solomon trench (see Figure 14). The formerly active North Solomon subduction is believed to have shut down due to the trench collision of the abnormally thick lithosphere of the Ontong Java Plateau. A hiatus in island arc volcanism (from late-early to early-late Miocene) is observed that correlates with the ~10 Ma long period of the subduction polarity reversal [*Coleman and Kroenke*, 1981]. The lack of volcanism can be explained by the lack of a mantle wedge atop the subducting plate during the reversal that is due to the thick crust and lithosphere of the Ontong Java Plateau at the interface to the newly subducting Indo-Australian plate.

Our model does not account for the presence of a buoyant plateau: In the presented experiment, the subducting plate is gradually slowed down while the spreading center approaches the trench formed by subduction. The fact that it still leads to a polarity reversal indicates that the slowing of the subducting plate might not need to be as abrupt as in the case of an oceanic plateau collision. The width between the North Solomon trench of the inactive subduction zone that dips toward the southwest and the San Cristobal trench of the active subduction zone that dips toward the northeast is around 260 km. This is in agreement with our model result and corresponds to the lateral extent of the wedge of accumulated weak material atop the subduction zone.

Subduction shut-off in the models presented here coincides with the termination of the mobile-lid regime due to the spatial limitations imposed by the 2-D modeling domain (i.e., there is only one active subduction zone at a time). In contrast, multiple subduction zones operate simultaneously in the 3-D shell of the Earth's mantle. The shutdown of one subduction zone does therefore not necessarily terminate a mobile lid in nature, and therefore on Earth, many examples exist which characterize the dynamics of subduction termination.

The combination of an approaching spreading ridge and then slab break-off, as observed in our experiments, is believed to have happened along the Baja California Sur plate boundary [*Michaud et al.*, 2006] and in the Patagonian part of the Andean collision zone, as shown in Figure 15 [*Guivel et al.*, 2006]. In the latter example, the ridge segment approached the subduction trench (after a period of ongoing plate convergence), which increased the tectonic coupling between the subducting and the overriding plates.

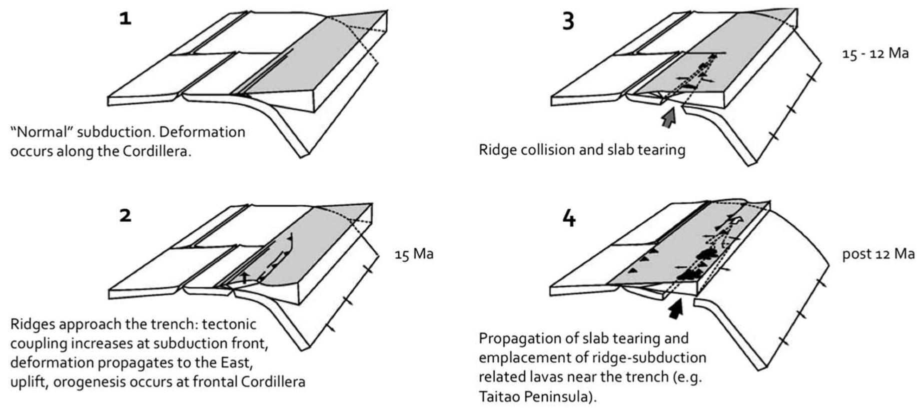

Figure 15. Cartoon showing the main stages of the proposed tectonic model of slab tearing during ridge collision at the trench for the most southern part of the Andean collision zone. Figure is reproduced from *Guivel et al.* [2006].

This led to deformation in the upper plate and to resistance against further sinking of the downgoing plate. After the ridge collision with the trench, the slab started to break off deeper in the subduction zone, leaving at the surface a young segment that was previously part of the subducting plate. This slab tearing is thereby related to the emplacement of alkali basalt and ridge-subduction-related lavas near the trench at the surface (e.g., Taitao Peninsula).

4. Conclusions

The goal of this study is to gain new knowledge concerning the key parameters shaping global-scale dynamics, using a simplified modeling approach. The model presented here is thus in no way an exact replica of a rocky planet like the Earth, and there will always be both agreement and disagreement between model features and nature.

We use a dynamically self-consistent modeling approach for the mantle plate system with a free outer surface, which is key in producing time-dependent, single-sided subduction like that found in nature [*Crameri et al.*, 2012a; *Crameri and Tackley*, 2014]. This enables more realistic numerical experiments that are able to self-consistently produce observed plate tectonics features such as subduction polarity reversals. In this study, the influence of different physical parameters and complexities, as well as some idealizations associated with numerical implementation, are tested.

We first contrast models containing the widely used free-slip upper boundary to models with a free surface. A dramatic difference in subduction dynamics is apparent, due to the free surface cases displaying many episodes of single-sided subduction: Single-sided subduction leads to more realistic (i) slab dip, (ii) stress state inside the slab, (iii) plate velocities, (iv) slab effective viscosity in the bending region, (v) trench retreat rates, (vi) slab-induced mantle flow, and (vii) back-arc spreading.

However, the single-sided subduction is often temporally unstable; several parameters are important for making it long lived (stable). Particularly important are (i) an appropriate yield stress (too high and subduction stops; too low and blob-like subduction occurs), (ii) a layer of weak hydrated crust approximated by a low yield stress, which efficiently lubricates the subduction channel, (iii) a high viscosity contrast between plates and the sublithospheric mantle, which helps the slab and connected surface plate to behave as one connected unit, and (iv) a low-viscosity asthenosphere, which is important for the lubrication of plates. For a reliable numerical solution it is essential to have (v) a suitably low sticky air viscosity (the criterion from [*Crameri et al.*, 2012b] works well in predicting what is necessary) and (vi) high enough spatial resolution to resolve the weak subduction channel.

In cases with ongoing single-sided subduction we observe some interesting behavior, particularly subduction polarity reversal, which generally occurs once the overriding plate becomes thick and hence convectively unstable, and subduction shut-off, which is caused either by a spreading center reaching the subduction zone or by a reduction of slab pull due to piling up subducted slab in the deep mantle and is associated with slab break-off.

Some model features are not in good agreement with natural observations, including (i) the lithospheric thickness—slightly too large due to a lower than Earth-like Rayleigh number, (ii) the strength (effective viscosity) of deep subducted slabs, which appears too high compared to observationally inferred values; this could be due to the lack of an additional high-pressure deformation mechanism and/or lack of recrystallization to small grain size due to phase transitions and (iii) the low friction coefficient needed to obtain mobile-lid behavior, which is substantially lower than laboratory-measured values [*Kohlstedt et al.*, 1995]. The latter discrepancy is common to all dynamically self-consistent mantle convection models without preset artificial weak zones and also to models in which the location of weak zones is specified. One weakening mechanism that might help to account for this discrepancy is weakening of oceanic lithosphere caused by hydration and serpentinization, due to either thermal cracking [*Korenaga*, 2007] or bending [*Faccenda et al.*, 2012]. However, this may not be applicable to the central parts of wide plates (e.g., the central Pacific plate), since *Zhong and Watts* [2013] inferred from a comparison between model results and observations of lithospheric flexure and seismicity (caused by the Hawaiian islands loading) that the friction coefficient inside the oceanic lithosphere is $\mu > 0.25$.

Disagreements between model and nature might be caused by the simplifications and associated assumptions that are made in the model. A first major assumption is (i) the absence of important 3-D mantle flow. Models run in 2-D space effectively represent infinitely wide subduction zones and neglect the important effect of variable trench width [*Stegman et al.*, 2006], possible 3-D influences on slab-sinking resistance [*Li and Ribe*, 2012] or overriding plate deformation [*Schellart and Moresi*, 2013], and any toroidal motion like trench-parallel flow beneath the slab [e.g., *Buttles and Olson*, 1998; *Kincaid and Griffiths*, 2003] or the return flow around slab edges [*Funiciello et al.*, 2006] caused by slab retreat. Additionally, there are some important aspects due to the sphericity of a planet that might not be captured by experiments in Cartesian model domains [e.g., *O'Farrell and Lowman*, 2010]. Models run in 3-D and fully spherical geometry accounting for these aspects are discussed and presented in *Crameri and Tackley* [2014]. Further major assumptions made in the model presented here are (ii) the incompressibility of the mantle (the Boussinesq approximation), which for example eliminates shear heating, (iii) the inelasticity of the rocks, (iv) the compositionally homogeneous lithosphere (i.e., no continents), (v) no history-dependent rheology, such as is given by grain size evolution, (vi) no basal heating (which would give plumes) and the presence of constant internal heating, (vii) the lower than Earth-like Rayleigh number (i.e., the less vigorous convection), (viii) including only diffusion creep and brittle plastic failure as deformation mechanisms, and (ix) the absence of sharp phase changes (e.g., upper mantle transition zone). The influence of these factors on mobile-lid tectonics with a free surface should be investigated in future studies.

The computationally efficient and time-dependent numerical model, a viscoplastic rheology, and a free surface allow us to reproduce the first-order characteristics of the differential drift of surface plates on top of a convecting mantle. Weak hydrated crust, a low-viscosity asthenosphere, and strong slabs promote the longevity of single-sided subduction, which then can even develop dramatic polarity reversals and slab break-offs. Models like these will be essential for our quest to a more robust understanding of Earth's dynamic evolution.

Acknowledgments
We thank the associate editor Wouter Schellart, Julian Lowman, and an anonymous reviewer for careful and constructive reviews. This work was supported by SNF grant 20TO21-120535 as part of the TOPO-EUROPE program. Some calculations were performed on ETHs Brutus high-performance computing cluster. Further methodical details and the raw numerical data can be requested from the author (www.fabiocrameri.ch).

References

Amstutz, A. (1955), Structures alpines; subductions successives dans l'Ossola, Comptes Rendus Hebdomadaires des Seances de l'Academie des, *Sciences*, *241*(15), 967–969, subduction, a term introduced by Andre Amstutz (1951, p. 326).

Bellahsen, N., C. Faccenna, and F. Funiciello (2005), Dynamics of subduction and plate motion in laboratory experiments: Insights into the "plate tectonics" behavior of the Earth, *J. Geophys. Res.*, *110*, B01401, doi:10.1029/2004JB002999.

Bercovici, D. (1998), Generation of plate tectonics from lithosphere-mantle flow and void-volatile self-lubrication, *Earth Planet. Sci. Lett.*, *154*(1–4), 139–151.

Bercovici, D., and Y. Ricard (2005), Tectonic plate generation and two-phase damage: Void growth versus grain size reduction, *J. Geophys. Res.*, *110*, B03401, doi: 10.1029/2004JB003181.

Bercovici, D., and Y. Ricard (2013), Generation of plate tectonics with two-phase grain-damage and pinning: Source–sink model and toroidal flow, *Earth Planet. Sci. Lett.*, *365*, 275–288.

Bercovici, D., Y. Ricard, and M. A. Richards (2000), The relation between mantle dynamics and plate tectonics: A primer, in *The History and Dynamics of Global Plate Motions, Geophys. Monogr. Ser.*, vol. 121, edited by M. A. Richards, R. G. Gordon, and R. D. Van Der Hilst, pp. 5–46, AGU, Washington, D. C.

Bijwaard, H., W. Spakman, and E. R. Engdahl (1998), Closing the gap between regional and global travel time tomography, *J. Geophys. Res.*, *103*(B12), 30,055–30,078.

Billen, M. I., M. Gurnis, and M. Simons (2003), Multiscale dynamics of the Tonga-Kermadec subduction zone, *Geophys. J. Int.*, *153*(2), 359–388.

Bird, P. (2003), An updated digital model of plate boundaries, *Geochem. Geophys. Geosyst.*, *4*(3), 1027, doi:10.1029/2001GC000252.

Bunge, H.-P., and M. A. Richards (1996), The origin of large scale structure in mantle convection: Effects of plate motions and viscosity stratification, *Geophys. Res. Lett.*, *23*(21), 2987–2990.

Bunge, H.-P., M. A. Richards, and J. R. Baumgardner (2002), Mantle-circulation models with sequential data assimilation: Inferring present-day mantle structure from plate-motion histories, *Philos. Trans. R. Soc. London, Ser. A*, *360*(1800), 2545–2567.

Burkett, E. R., and M. I. Billen (2010), Three-dimensionality of slab detachment due to ridge-trench collision: Laterally simultaneous boudinage versus tear propagation, *Geochem. Geophys. Geosyst.*, *11*, Q11012, doi:10.1029/2010GC003286.

Butterworth, N. P., L. Quevedo, G. Morra, and R. D. Müller (2012), Influence of overriding plate geometry and rheology on subduction, *Geochem. Geophys. Geosyst.*, *13*, Q06W15.

Buttles, J., and P. Olson (1998), A laboratory model of subduction zone anisotropy, *Earth Planet. Sci. Lett.*, *164*(1–2), 245–262.

Capitanio, F., G. Morra, and S. Goes (2007), Dynamic models of downgoing plate-buoyancy driven subduction: Subduction motions and energy dissipation, *Earth Planet. Sci. Lett.*, *262*(1–2), 284–297.

Capitanio, F., D. Stegman, L. Moresi, and W. Sharples (2010), Upper plate controls on deep subduction, trench migrations and deformations at convergent margins, *Tectonophysics*, *483*(1–2), 80–92, doi:10.1016/j.tecto.2009.08.020, convergent plate margin dynamics: New perspectives from structural geology, geophysics and geodynamic modelling.

Capitanio, F. A., G. Morra, and S. Goes (2009), Dynamics of plate bending at the trench and slab-plate coupling, *Geochem. Geophys. Geosyst.*, *10*, Q04002, doi:10.1029/2008GC002348.

Capitanio, F. A., C. Faccenna, S. Zlotnik, and D. R. Stegman (2011), Subduction dynamics and the origin of andean orogeny and the Bolivian orocline, *Nature*, *480*, 83–86, doi:10.1038/nature10596.

Chase, C. G. (1979), Asthenospheric counterflow: A kinematic model, *Geophys. J. R. Astron. Soc.*, *56*(1), 1–18.

Clark, S. R., D. Stegman, and R. D. Müller (2008), Episodicity in back-arc tectonic regimes, *Phys. Earth Planet. Inter.*, *171*(1–4), 265–279.

Cloos, M., and R. L. Shreve (1988), Subduction-channel model of prism accretion, melange formation, sediment subduction, and subduction erosion at convergent plate margins: 1. Background and description, *Pure Appl. Chem.*, *128*(3–4), 455–500.

Coleman, P., and L. Kroenke (1981), Subduction without volcanism in the Solomon Islands arcs, *Geo-Mar. Lett.*, *1*(2), 129–134.

Cooper, P. A., and B. Taylor (1985), Polarity reversal in the Solomon Islands arc, *Nature*, *314*, 428–430.

Crameri, F. (2013), The interaction between subduction-related mantle currents and surface topography, PhD thesis, ETH Zurich, Zurich, Switzerland, doi:10.3929/ethz-a-009954311.

Crameri, F., and B. J. P. Kaus (2010), Parameters that control lithospheric-scale thermal localization on terrestrial planets, *Geophys. Res. Lett.*, *37*, L09308, doi:10.1029/2010GL042921.

Crameri, F., and P. J. Tackley (2014), Spontaneous development of arcuate single-sided subduction in global 3-D mantle convection models with a free surface, *J. Geophys. Res. Solid Earth*, *119*, 5921–5942, doi:10.1002/2014JB010939.

Crameri, F., P. J. Tackley, I. Meilick, T. V. Gerya, and B. J. P. Kaus (2012a), A free plate surface and weak oceanic crust produce single-sided subduction on Earth, *Geophys. Res. Lett.*, *39*, L03306, doi:10.1029/2011GL050046.

Crameri, F., H. Schmeling, G. J. Golabek, T. Duretz, R. Orendt, S. J. H. Buiter, D. A. May, B. J. P. Kaus, T. V. Gerya, and P. J. Tackley (2012b), A comparison of numerical surface topography calculations in geodynamic modelling: An evaluation of the 'sticky air' method, *Geophys. J. Int.*, *189*(1), 38–54, doi:10.1111/j.1365-246X.2012.05388.x.

Davies, G. F. (1989), Mantle convection model with a dynamic plate: Topography, heat flow and gravity anomalies, *Geophys. J. Int.*, *98*(3), 461–464.

Davies, J. H., and D. J. Stevenson (1992), Physical model of source region of subduction zone volcanics, *J. Geophys. Res.*, *97*(B2), 2037–2070.

De Franco, R., R. Govers, and R. Wortel (2007), Numerical comparison of different convergent plate contacts: Subduction channel and subduction fault, *Geophys. J. Int.*, *171*(1), 435–450.

de Wit, M. J. (1998), On Archean granites, greenstones, cratons and tectonics: Does the evidence demand a verdict?, *Precambrian Res.*, *91*(1–2), 181–226, doi:10.1016/S0301-9268(98)00043-6.

Duarte, J. C., W. P. Schellart, and A. R. Cruden (2013), Three-dimensional dynamic laboratory models of subduction with an overriding plate and variable interplate rheology, *Geophys. J. Int.*, *195*, 47–66.

Duretz, T., T. V. Gerya, and D. A. May (2011), Numerical modelling of spontaneous slab breakoff and subsequent topographic response, *Tectonophysics*, *502*(1–2), 244–256.

Dvorkin, J., A. Nur, G. Mavko, and Z. Ben-Avraham (1993), Narrow subducting slabs and the origin of backarc basins, *Tectonophysics*, *227*(1–4), 63–79.

Dymkova, D., and T. Gerya (2013), Porous fluid flow enables oceanic subduction initiation on Earth, *Geophys. Res. Lett.*, *40*, 5671–5676, doi:10.1002/2013GL057798.

Faccenda, M., T. V. Gerya, N. S. Mancktelow, and L. Moresi (2012), Fluid flow during slab unbending and dehydration: Implications for intermediate-depth seismicity, slab weakening and deep water recycling, *Geochem. Geophys. Geosyst.*, *13*, Q01010, doi:10.1029/2011GC003860.

Foley, B. J., and T. W. Becker (2009), Generation of plate-like behavior and mantle heterogeneity from a spherical, viscoplastic convection model, *Geochem. Geophys. Geosyst.*, *10*, Q08001, doi:10.1029/2009GC002378.

Foley, B. J., and D. Bercovici (2014), Scaling laws for convection with temperature-dependent viscosity and grain-damage, *Geophys. J. Int.*, *199*(1), 580–603.

Fowler, A. C. (1985), Fast thermoviscous convection, *Stud. Appl. Math.*, *72*, 189–219.

Fukao, Y., S. Widiyantoro, and M. Obayashi (2001), Stagnant slabs in the upper and lower mantle transition region, *Rev. Geophys.*, *39*(3), 291–323.

Funiciello, F., M. Moroni, C. Piromallo, C. Faccenna, A. Cenedese, and H. A. Bui (2006), Mapping mantle flow during retreating subduction: Laboratory models analyzed by feature tracking, *J. Geophys. Res.*, *111*, B03402, doi:10.1029/2005JB003792.

Funiciello, F., C. Faccenna, A. Heuret, S. Lallemand, E. Di Giuseppe, and T. Becker (2008), Trench migration, net rotation and slab-mantle coupling, *Earth Planet. Sci. Lett.*, *271*(1–4), 233–240.

Gait, A. D., J. P. Lowman, and C. W. Gable (2008), Time dependence in 3-D mantle convection models featuring evolving plates: Effect of lower mantle viscosity, *J. Geophys. Res.*, *113*, B08409, doi:10.1029/2007JB005538.

Garel, F., S. Goes, D. R. Davies, J. H. Davies, S. C. Kramer, and C. R. Wilson (2014), Interaction of subducted slabs with the mantle transition-zone: A regime diagram from 2-D thermo-mechanical models with a mobile trench and an overriding plate, *Geochem. Geophys. Geosyst.*, *15*, 1739–1765, doi:10.1002/2014GC005257.

Gerya, T. (2011), Future directions in subduction modeling, *J. Geodyn.*, *52*(5), 344–378.

Gerya, T. V., J. A. Connolly, and D. A. Yuen (2008), Why is terrestrial subduction one-sided?, *Geology*, *36*(1), 43–46, doi:10.1130/G24060A.1.

Guivel, C., et al. (2006), Miocene to Late Quaternary Patagonian basalts (46–47°S): Geochronometric and geochemical evidence for slab tearing due to active spreading ridge subduction, *J. Volcanol. Geotherm. Res.*, *149*(3–4), 346–370.

Gurnis, M. (1988), Large-scale mantle convection and the aggregation and dispersal of supercontinents, *Nature*, *332*(6166), 695–699.

Hager, B. H., and R. J. O'Connell (1979), Kinematic models of large-scale flow in the Earth's mantle, *J. Geophys. Res.*, *84*(B3), 1031–1048.

Hirth, G., and D. Kohlstedt (2003), Rheology of the upper mantle and the mantle wedge: A view from the experimentalists, in *Inside the Subduction Factory, Geophys. Monogr. Ser.*, vol. 138, edited by J. Eiler, pp. 83–105, AGU, Washington, D. C.

Höink, T., A. Lenardic, and M. Richards (2012), Depth-dependent viscosity and mantle stress amplification: Implications for the role of the asthenosphere in maintaining plate tectonics, *Geophys. J. Int.*, *191*(1), 30–41.

Irvine, D. N., and W. P. Schellart (2012), Effect of plate thickness on bending radius and energy dissipation at the subduction zone hinge, *J. Geophys. Res.*, *117*, B06405, doi:10.1029/2011JB009113.

Karato, S.-I., M. Toriumi, and T. Fujii (1980), Dynamic recrystallization of olivine single crystals during high-temperature creep, *Geophys. Res. Lett.*, *7*(9), 649–652.

Karato, S.-I., M. S. Paterson, and J. D. FitzGerald (1986), Rheology of synthetic olivine aggregates: Influence of grain size and water, *J. Geophys. Res.*, *91*(B8), 8151–8176.

Kaus, B. J., H. Mühlhaus, and D. A. May (2010), A stabilization algorithm for geodynamic numerical simulations with a free surface, *Phys. Earth Planet. Inter.*, *181*(1–2), 12–20, doi:10.1016/j.pepi.2010.04.007.

Kelemen, P. B., and G. Hirth (2007), A periodic shear-heating mechanism for intermediate-depth earthquakes in the mantle, *Nature*, *446*, 787–790.

Kincaid, C., and R. W. Griffiths (2003), Laboratory models of the thermal evolution of the mantle during rollback subduction, *Nature*, *425*(6953), 58–62.

King, S. D. (2001), Subduction zones: Observations and geodynamic models, *Phys. Earth Planet. Inter.*, *127* (1–4), 9–24, doi:10.1016/S0031-9201(01)00218-7.

King, S. D., and B. H. Hager (1990), The relationship between plate velocity and trench viscosity in Newtonian and power-law subduction calculations, *Geophys. Res. Lett.*, *17*(13), 2409–2412.

King, S. D., J. P. Lowman, and C. W. Gable (2002), Episodic tectonic plate reorganizations driven by mantle convection, *Earth Planet. Sci. Lett.*, *203*(1), 83–91.

Kohlstedt, D. L., B. Evans, and S. J. Mackwell (1995), Strength of the lithosphere: Constraints imposed by laboratory experiments, *J. Geophys. Res.*, *100*(B9), 17,587–17,602.

Korenaga, J. (2007), Thermal cracking and the deep hydration of oceanic lithosphere: A key to the generation of plate tectonics?, *J. Geophys. Res.*, *112*, B05408, doi:10.1029/2006JB004502.

Lallemand, S., A. Heuret, and D. Boutelier (2005), On the relationships between slab dip, back-arc stress, upper plate absolute motion, and crustal nature in subduction zones, *Geochem. Geophys. Geosyst.*, *6*, Q09006, doi:10.1029/2005GC000917.

Lenardic, A., and W. M. Kaula (1994), Self-lubricated mantle convection: Two-dimensional models, *Geophys. Res. Lett.*, *21*(16), 1707–1710.

Li, Z.-H., and N. M. Ribe (2012), Dynamics of free subduction from 3-D boundary element modeling, *J. Geophys. Res.*, *117*, B06408, doi:10.1029/2012JB009165.

Lowman, J. P. (2011), Mantle convection models featuring plate tectonic behavior: An overview of methods and progress, *Tectonophysics*, *510*(1–2), 1–16.

Matsumoto, T., and Y. Tomoda (1983), Numerical simulation of the initiation of subduction at the fracture zone, *J. Phys. Earth*, *31*(3), 183–194.

McKenzie, D. P. (1969), Speculations on the consequences and causes of plate motions, *Geophys. J. Int.*, *18*(1), 1–32.

Meyer, C., and W. P. Schellart (2013), Three-dimensional dynamic models of subducting plate-overriding plate-upper mantle interaction, *J. Geophys. Res. Solid Earth*, *118*, 775–790, doi:10.1002/jgrb.50078.

Michaud, F., et al. (2006), Oceanic-ridge subduction vs. slab break off: Plate tectonic evolution along the Baja California Sur continental margin since 15 Ma, *Geology*, *34*(1), 13–16.

Mishin, Y. A., T. V. Gerya, J.-P. Burg, and J. A. Connolly (2008), Dynamics of double subduction: Numerical modeling, *Phys. Earth Planet. Inter.*, *171*(1–4), 280–295, doi:10.1016/j.pepi.2008.06.012.

Monnereau, M., and S. Quéré (2001), Spherical shell models of mantle convection with tectonic plates, *Earth Planet. Sci. Lett.*, *184*(3–4), 575–587.

Moresi, L., and M. Gurnis (1996), Constraints on the lateral strength of slabs from three-dimensional dynamic flow models, *Earth Planet. Sci. Lett.*, *138*(1–4), 15–28.

Moresi, L., and V. Solomatov (1998), Mantle convection with a brittle lithosphere: Thoughts on the global tectonic styles of the Earth and Venus, *Geophys. J. Int.*, *133*(3), 669–682.

Nataf, H., and F. Richter (1982), Convection experiments in fluids with highly temperature-dependent viscosity and the thermal evolution of the planets, *Phys. Earth Planet. Inter.*, *29*(3–4), 320–329.

O'Farrell, K. A., and J. P. Lowman (2010), Emulating the thermal structure of spherical shell convection in plane-layer geometry mantle convection models, *Phys. Earth Planet. Inter.*, *182*(1–2), 73–84.

Peacock, S. M. (1990), Numerical simulation of metamorphic pressure-temperature-time paths and fluid production in subducting slabs, *Tectonics*, *9*(5), 1197–1211.

Puster, P., B. H. Hager, and T. H. Jordan (1995), Mantle convection experiments with evolving plates, *Geophys. Res. Lett.*, *22*(16), 2223–2226.

Quinquis, M. E. T., S. J. H. Buiter, and S. Ellis (2011), The role of boundary conditions in numerical models of subduction zone dynamics, *Tectonophysics*, *497*(1–4), 57–70, doi:10.1016/j.tecto.2010.11.001.

Ratcliff, J. T., P. J. Tackley, G. Schubert, and A. Zebib (1997), Transitions in thermal convection with strongly variable viscosity, *Phys. Earth Planet. Inter.*, *102*(3–4), 201–212.

Regenauer-Lieb, K. (1998), Dilatant plasticity applied to Alpine collision: Ductile void growth in the intraplate area beneath the Eifel volcanic field, *J. Geodyn.*, *27*(1), 1–21.

Ribe, N. M. (2010), Bending mechanics and mode selection in free subduction: A thin-sheet analysis, *Geophys. J. Int.*, *180*(2), 559–576.

Richards, M. A., W.-S. Yang, J. R. Baumgardner, and H.-P. Bunge (2001), Role of a low-viscosity zone in stabilizing plate tectonics: Implications for comparative terrestrial planetology, *Geochem. Geophys. Geosyst.*, *2*(8), 1026.

Riedel, M. R., and S.-i. Karato (1997), Grain-size evolution in subducted oceanic lithosphere associated with the olivine-spinel transformation and its effects on rheology, *Earth Planet. Sci. Lett.*, *148*(1–2), 27–43.

Rolf, T., and P. J. Tackley (2011), Focussing of stress by continents in 3D spherical mantle convection with self-consistent plate tectonics, *Geophys. Res. Lett.*, *38*, L18301, doi:10.1029/2011GL048677.

Rozel, A., Y. Ricard, and D. Bercovici (2011), A thermodynamically self-consistent damage equation for grain size evolution during dynamic recrystallization, *Geophys. J. Int.*, *184*(2), 719–728.

Samowitz, I. R., and D. W. Forsyth (1981), Double seismic zone beneath the Mariana Island Arc, *J. Geophys. Res.*, *86*(B8), 7013–7021.

Schellart, W. (2009), Evolution of the slab bending radius and the bending dissipation in three-dimensional subduction models with a variable slab to upper mantle viscosity ratio, *Earth Planet. Sci. Lett.*, *288*(1–2), 309–319.

Schellart, W., D. Stegman, and J. Freeman (2008), Global trench migration velocities and slab migration induced upper mantle volume fluxes: Constraints to find an Earth reference frame based on minimizing viscous dissipation, *Earth Sci. Rev.*, *88*(1–2), 118–144.

Schellart, W. P. (2008a), Subduction zone trench migration: Slab driven or overriding-plate-driven?, *Phys. Earth Planet. Inter.*, *170*(1–2), 73–88.

Schellart, W. P. (2008b), Kinematics and flow patterns in deep mantle and upper mantle subduction models: Influence of the mantle depth and slab to mantle viscosity ratio, *Geochem. Geophys. Geosyst.*, *9*, Q03014, doi:10.1029/2007GC001656.

Schellart, W. P., and L. Moresi (2013), A new driving mechanism for backarc extension and backarc shortening through slab-sinking-induced toroidal and poloidal mantle flow: Results from dynamic subduction models with an overriding plate, *J. Geophys. Res. Solid Earth*, *118*(6), 3221–3248, doi:10.1002/jgrb.50173.

Schmeling, H., and W. Jacoby (1981), On modelling the lithosphere in mantle convection with nonlinear rheology, *J. Geophys.*, *50*, 89–100.

Schmeling, H., et al. (2008), A benchmark comparison of spontaneous subduction models—Towards a free surface, *Phys. Earth Planet. Inter.*, *171*(1–4), 198–223, doi:10.1016/j.pepi.2008.06.028.

Schmidt, M. W., and S. Poli (1998), Experimentally based water budgets for dehydrating slabs and consequences for arc magma generation, *Earth Planet. Sci. Lett.*, *163*(1–4), 361–379, doi:10.1016/S0012-821X(98)00142-3.

Sdrolias, M., and R. D. Müller (2006), Controls on back-arc basin formation, *Geochem. Geophys. Geosyst.*, *7*, Q04016, doi:10.1029/2005GC001090.

Sizova, E., T. Gerya, M. Brown, and L. Perchuk (2010), Subduction styles in the Precambrian: Insight from numerical experiments, *Lithos*, *116*(3–4), 209–229, doi:10.1016/j.lithos.2009.05.028.

Smith, W. H. F., and D. T. Sandwell (1997), Global sea floor topography from satellite altimetry and ship depth soundings, *Science*, *277*(5334), 1956–1962, doi:10.1126/science.277.5334.1956.

Solomatov, V. S. (1995), Scaling of temperature- and stress-dependent viscosity convection, *Physics of Fluids*, *7*, 266.

Solomatov, V. S. (2004), Initiation of subduction by small-scale convection, *J. Geophys. Res.*, *109*, B01412, doi:10.1029/2003JB002628.

Stegman, D., R. Farrington, F. Capitanio, and W. Schellart (2010), A regime diagram for subduction styles from 3-D numerical models of free subduction, *Tectonophysics*, *483*(1–2), 29–45.

Stegman, D. R., J. Freeman, W. P. Schellart, L. Moresi, and D. May (2006), Influence of trench width on subduction hinge retreat rates in 3-D models of slab rollback, *Geochem. Geophys. Geosyst.*, *7*, Q03012, doi:10.1029/2005GC001056.

Stein, C., J. Schmalzl, and U. Hansen (2004), The effect of rheological parameters on plate behaviour in a self-consistent model of mantle convection, *Phys. Earth Planet. Inter.*, *142*, 225–255.

Steinberger, B., R. Sutherland, and R. J. O'connell (2004), Prediction of Emperor-Hawaii seamount locations from a revised model of global plate motion and mantle flow, *Nature*, *430*(6996), 167–173.

Stengel, K. C., D. S. Oliver, and J. R. Booker (1982), Onset of convection in a variable-viscosity fluid, *J. Fluid Mech.*, *120*, 411–431, doi:10.1017/S0022112082002821.

Stevenson, D., and J. Turner (1977), Angle of subduction, *Nature*, *270*, 334–336.

Tackley, P. J. (2000a), Self-consistent generation of tectonic plates in time-dependent, three-dimensional mantle convection simulations – Part 1: Pseudo-plastic yielding, *Geochem. Geophys. Geosyst.*, *1*(8), 1525.

Tackley, P. J. (2000b), Self-consistent generation of tectonic plates in time-dependent, three-dimensional mantle convection simulations – Part 2: Strain weakening and asthenosphere, *Geochem. Geophys. Geosyst.*, *1*, 1026.

Tackley, P. J. (2008), Modelling compressible mantle convection with large viscosity contrasts in a three-dimensional spherical shell using the yin-yang grid, *Phys. Earth Planet. Inter.*, *171*(1–4), 7–18, doi:10.1016/j.pepi.2008.08.005.

Tagawa, M., T. Nakakuki, M. Kameyama, and F. Tajima (2007), The role of history-dependent rheology in plate boundary lubrication for generating one-sided subduction, *Pure Appl. Geophys.*, *164*(5), 879–907.

Taylor, B., and G. D. Karner (1983), On the evolution of marginal basins, *Rev. Geophys.*, *21*(8), 1727–1741.

Thielmann, M., and B. J. Kaus (2012), Shear heating induced lithospheric-scale localization: Does it result in subduction?, *Earth Planet. Sci. Lett.*, *359–360*, 1–13.

Toksöz, M., and A. T. Hsui (1978), Numerical studies of back-arc convection and the formation of marginal basins, *Tectonophysics*, *50*(2–3), 177–196.

Trompert, R., and U. Hansen (1998), Mantle convection simulations with rheologies that generate plate-like behaviour, *Nature*, *395*, 686–689.

van Dinther, Y., G. Morra, F. Funiciello, and C. Faccenna (2010), Role of the overriding plate in the subduction process: Insights from numerical models, *Tectonophysics*, *484*(1–4), 74–86.

van Heck, H. J., and P. J. Tackley (2008), Planforms of self-consistently generated plates in 3D spherical geometry, *Geophys. Res. Lett.*, *35*, L19312, doi:10.1029/2008GL035190.

van Hunen, J., and M. B. Allen (2011), Continental collision and slab break-off: A comparison of 3-D numerical models with observations, *Earth Planet. Sci. Lett.*, *302*(1–2), 27–37.

van Hunen, J., and A. P. van den Berg (2008), Plate tectonics on the early Earth: Limitations imposed by strength and buoyancy of subducted lithosphere, *Lithos*, *103*(1–2), 217–235, doi:10.1016/j.lithos.2007.09.016.

Čížková, H., J. van Hunen, and A. van den Berg (2007), Stress distribution within subducting slabs and their deformation in the transition zone, *Phys. Earth Planet. Inter.*, *161*(3–4), 202–214.

Wortel, M. J. R., and W. Spakman (2000), Subduction and slab detachment in the Mediterranean-Carpathian region, *Science*, *290*(5498), 1910–1917, doi:10.1126/science.290.5498.1910.

Wu, B., C. P. Conrad, A. Heuret, C. Lithgow-Bertelloni, and S. Lallemand (2008), Reconciling strong slab pull and weak plate bending: The plate motion constraint on the strength of mantle slabs, *Earth Planet. Sci. Lett.*, *272*(1–2), 412–421.

Yamato, P., L. Husson, J. Braun, C. Loiselet, and C. Thieulot (2009), Influence of surrounding plates on 3D subduction dynamics, *Geophys. Res. Lett.*, *36*, L07303, doi:10.1029/2008GL036942.

Yuen, D. A., L. Fleitout, G. Schubert, and C. Froidevaux (1978), Shear deformation zones along major transform faults and subducting slabs, *Geophys. J. R. Astron. Soc.*, *54*(1), 93–119.

Zhao, D. (2004), Global tomographic images of mantle plumes and subducting slabs: Insight into deep Earth dynamics, *Phys. Earth Planet. Inter.*, *146*(1–2), 3–34, doi:10.1016/j.pepi.2003.07.032.

Zhong, S., and M. Gurnis (1995), Towards a realistic simulation of plate margins in mantle convection, *Geophys. Res. Lett.*, *22*(8), 981–984.

Zhong, S., and M. Gurnis (1996), Interaction of weak faults and non-Newtonian rheology produces plate tectonics in a 3D model of mantle flow, *Nature*, *383*, 245–247, doi:10.1038/383245a0.
Zhong, S., and A. B. Watts (2013), Lithospheric deformation induced by loading of the Hawaiian Islands and its implications for mantle rheology, *J. Geophys. Res. Solid Earth*, *118*, 6025–6048, doi:10.1002/2013JB010408.
Zhong, S., M. Gurnis, and L. Moresi (1998), Role of faults, nonlinear rheology, and viscosity structure in generating plates from instantaneous mantle flow models, *J. Geophys. Res.*, *103*(B7), 15,255–15,268.

